CANCER

Image-guided targeting of mitochondrial metabolism sensitizes pediatric malignant rhabdoid tumors to low-dose radiotherapy

Wenxi Xia[1], Esther Need[1], Carmine Schiavone[2,3], Neetu Singh[1], Jiemin Huang[1], Matthew Goff[1], Joseph Cave[2,4], David L. Gillespie[5], Randy L. Jensen[5], Mark D. Pagel[6], Prashant Dogra[2,7], Sixiang Shi[1,8]*, Shreya Goel[1,8,9]*

Tumor hypoxia leads to radioresistance and markedly worse clinical outcomes for pediatric malignant rhabdoid tumors (MRTs). Our transcriptomics and bioenergetic profiling data reveal that mitochondrial oxidative phosphorylation is a metabolic vulnerability of MRT and can be exploited to overcome consumptive hypoxia by repurposing an FDA-approved antimalarial drug, atovaquone (AVO). We then establish the utility of oxygen-enhanced-multispectral optoacoustic tomography, a label-free, ionizing radiation-free imaging modality, to visualize and quantify spatiotemporal changes in tumor hypoxia in response to AVO. We show a potent but transient increase in tumor oxygenation upon AVO treatment that results in complete elimination of tumors in all tested mice when combined with 10-gray radiotherapy, a dose several times lower than the current clinic standard. Last, we use translational mathematical modeling for systematic evaluation of dosing regimens, administration timing, and therapeutic synergy in a virtual patient cohort. Together, our work establishes a framework for safe and pediatric patient-friendly image-guided metabolic radiosensitization of rhabdoid tumors.

INTRODUCTION

Malignant rhabdoid tumor (MRT) and atypical teratoid rhabdoid tumor (rhabdoid tumors occurring in the brain) are rare but one of the most lethal soft tissue cancers with a median overall survival ranging from 6 to 17 months (*1*), affecting infants and young children (*2*) with ~20 to 25 cases diagnosed each year in the US (*3*). Given the rarity of these malignancies, new drug discovery is scientifically and financially challenging. Three conventional treatments are commonly used for MRT, varying, in part, based on the disease stage: surgery, x-ray therapy (RT), and chemotherapy (*4*). Experimental treatment modalities including immunotherapy (*5*, *6*) and targeted therapy (*7*, *8*) are also being tested in preclinical trials (*9*). However, as most patients with MRT are younger than 3 years old, special considerations are associated with current treatments. For example, chemotherapy is initiated after surgery but not desirable because it is often associated with heterogeneous response and notable immediate and long-term toxicity in infant patients (*10*). All patients are treated with high dose localized RT. However, it is also associated with late-stage side effects such as growth and developmental delays in pediatric patients (*11*), as well as gastrointestinal dysfunction, pulmonary issues, infertility, cardiac abnormalities, and the potential for secondary cancers later in life (*12*). Thus, a safe and effective radiosensitizing adjuvant treatment that maximizes RT efficiency at lower doses and minimizes radiotoxicity can become a "game-changer" in pediatric MRT management.

Nearly all solid tumors suffer from diminished oxygen availability or tumor hypoxia (*13*), resulting from increased oxygen consumption because of high metabolic demand and inefficient oxygen delivery due to leaky and compressed vessels (*14*). Tumor hypoxia appears to be strongly associated with cancer progression, including epithelial-mesenchymal transition, tumor vascularization, angiogenesis, cell migration/invasion, metastasis, immunosuppression (*15*, *16*), as well as poor outcomes for various treatment modalities including RT, as oxygen acts as a potent radiosensitizer, enhancing the DNA damage caused by ionizing radiation (*17*, *18*). Therefore, attenuation of hypoxia may be a highly appealing strategy to enhance the sensitivity of tumors to radiation and thereby improve therapeutic outcomes in pediatric patients with MRT.

Now, there are two common strategies used to relieve tumor hypoxia: increasing oxygen delivery by exogenous routes or vascular remodeling, or reducing demand for oxygen by modulating cellular oxygen consumption rate (OCR) through metabolic reprogramming (*19*–*21*). Our transcriptomic profiling of MRT patient data in the TARGET database revealed a significant up-regulation of the oxidative phosphorylation (OXPHOS) pathways, suggesting that reducing hypoxia through OXPHOS inhibition could be a clinically feasible approach to enhance radiosensitivity in MRT treatment. Atovaquone (AVO), the first US Food and Drug Administration (FDA)–approved antimalarial and anti-pneumocystis pneumonia drug, was recently repurposed as an OXPHOS inhibitor for tumor growth suppression (*22*). AVO is proposed to reduce OCR by inhibiting the mitochondrial electron transport chain (ETC) at complex III, and studies have reported that AVO could effectively alleviate tumor hypoxia in various adult tumor types, as a monotherapy, as well as combination with radiotherapy and immunotherapy (*23*, *24*).

[1]Department of Molecular Pharmaceutics, University of Utah, Salt Lake City, UT 84112, USA. [2]Mathematics in Medicine Program, Department of Medicine, Houston Methodist Research Institute, Houston, TX 77030, USA. [3]Department of Chemical, Materials and Industrial Production Engineering, University of Naples Federico II, Naples, Italy. [4]Physiology, Biophysics, and Systems Biology Program, Graduate School of Medical Sciences, Weill Cornell Medicine, New York, NY 10065, USA. [5]Department of Neurosurgery, Huntsman Cancer Institute, University of Utah, Salt Lake City, UT 84132, USA. [6]Department of Medical Physics, University of Wisconsin-Madison, Madison, WI 53705, USA. [7]Department of Physiology and Biophysics, Weill Cornell Medical College, New York, NY 10065, USA. [8]Department of Radiology and Imaging Sciences, University of Utah, Salt Lake City, UT 84112, USA. [9]Department of Biomedical Engineering, University of Utah, Salt Lake City, UT 84112, USA. *Corresponding author. Email: sixiang.shi@utah.edu (S.S.); shreya.goel@utah.edu (S.G.)

We reasoned that AVO could be the game-changing radiosensitizer to enable effective treatment of pediatric solid tumors at lower radiation doses, which has not been tested yet.

To investigate the effectiveness of AVO in mouse models of pediatric MRT and characterize the extent and duration of hypoxia modulation, we used multispectral optoacoustic tomography (MSOT), a multiscale imaging modality to noninvasively visualize oxygenation and vascular perfusion at the tumor site (*25*–*27*). Data obtained at various wavelengths in optoacoustic tomography enables the quantification of oxy- and deoxyhemoglobin levels that can be used to measure oxygen saturation ($\%sO_2$) of the blood (*28*, *29*). By performing $\%sO_2$ measurement following a switch of respiration gas from air (21% oxygen) to 100% oxygen, using the oxygen-enhanced (OE-MSOT) procedure, ΔsO_2 can be measured, which represents the "available oxygen capacity" in the tumor (*30*). Additionally, dynamic contrast-enhanced (DCE)–MSOT can also be performed at the same time to evaluate tumor perfusion by analyzing NK^{trans} and K_{ep} pharmacokinetic parameters. These parameters, respectively, reflect the wash-in and washout perfusion rates of an FDA-approved agent, indocyanine green (ICG), within the tumor (*31*). Thus, OE- and DCE-MSOT together can provide quantitative, multiparametric, real-time functional information about tumor responses to administered AVO and RT in live animals.

In this work, we integrate whole body in vivo optoacoustic imaging and statistical parametric mapping with tissue-scale and cellular scale histological analysis to predict and assess the effectiveness of AVO-potentiated low-dose RT therapy in A-204 MRT xenografts (fig. S1). Our findings underscore the efficacy of OE-MSOT in mapping the spatiotemporal changes of drug pharmacodynamics, encouraging its use to guide personalized combination therapy regimens. Notably, our results indicate that, at low pharmacologically achievable concentrations, AVO can effectively but transiently alleviate hypoxia in A-204 tumors and strongly inhibit tumor growth in combination with a single 10-gray (Gy) x-ray dose with no adverse effects. These insights provide an important contribution toward pediatric MRT management in the clinic for which limited therapies exist. Further, to bridge the gap between preclinical findings and clinically applicable treatment regimens, mathematical modeling is used as a complementary approach to experimental investigations. By simulating tumor dynamics in virtual patient cohorts, the framework enabled a systematic evaluation of dosing regimens, administration timing, and therapeutic synergy. This approach identified optimal combination protocols to enhance clinical outcomes, guiding future studies and potentially supporting the translation of AVO as a radiosensitizer in MRT.

RESULTS

OXPHOS pathway is up-regulated in patients with clinical rhabdoid tumor

Tumor hypoxia plays a key role in increasing resistance to RT, leading to considerably worse clinical outcomes in pediatric MRT treatment. Thus, our objective here is to investigate targetable pathways that can reduce tumor hypoxia, enhance the effectiveness of RT, and minimize long-term radiotoxicity. Toward this end, we profiled transcriptomics data from 63 patients with rhabdoid cancer available from the Genomic Data Commons (GDC) database. The workflow for the RNA sequencing, pathway enrichment, and survival curve plotting are shown in Fig. 1A. After conducting single-sample gene set enrichment analysis (ssGSEA) on the transcriptomic data using Hallmark gene sets, we discovered that the OXPHOS pathway exhibited higher enrichment level compared to other pathways in patients with rhabdoid tumor, regardless of cancer stage (Fig. 1B). Therefore, we hypothesized that inhibiting OXPHOS could serve as an actionable strategy to augment RT by attenuating consumptive hypoxia. Additionally, to further understand which genes in the OXPHOS pathway influence survival rates, we performed Cox proportional hazards regression modeling on all OXPHOS-related genes and identified 11 genes with significant P values ($P < 0.05$; Fig. 1C), including genes associated with complex I and III activity in the ETC. As shown in Fig. 1D and fig. S2, survival curve analysis revealed that patients with high expression of UQCRFS1 (component of ubiquinol-cytochrome c oxidoreductase involved in complex III assembly) and NDUFA3 (involved in complex I assembly) had significantly lower survival rates compared to those with lower expression. Disrupting the complexes along the ETC is the most clinically viable way to pharmacologically target OXPHOS, and many OXPHOS inhibitors targeting complexes I and III are in various stages of clinical trials. AVO, a competitive inhibitor of ubiquinone, a crucial component of complex III [cytochrome bc1 complex; (*32*)], was selected in this study (Fig. 1E). AVO is an FDA-approved antiparasitic drug with well-established safety and efficacy profiles in both adults and children (*33*). AVO has been shown to inhibit OXPHOS at pharmacologically achievable concentrations in adult tumors (*34*).

AVO effectively alleviates hypoxia by inhibiting mitochondrial respiration via complex III in A-204 cells

To verify the inhibitory effect of AVO on mitochondrial respiration in pediatric MRT, we measured the OCRs in A-204 cells using a Seahorse XF Pro analyzer. Control groups treated with dimethyl sulfoxide (DMSO) alone were processed in parallel. Before measuring OCR traces, cytotoxicity experiments were conducted to determine the approximate AVO concentration for Seahorse experiments. As shown in Fig. 2A, AVO monotherapy did not exert substantial cytotoxicity on A-204 cells, yielding a median effective concentration (EC_{50}) value of ~28.36 μM. However, this concentration was sufficient to significantly suppress OXPHOS. Through the sequential injection of oligomycin, carbonyl cyanide *p*-trifluoromethoxyphenylhydrazone (FCCP), and rotenone/antimycin A, the basal respiration, maximal respiration, and adenosine 5′-triphosphate (ATP) production of A-204 cells were recorded, respectively. OCR traces shown in Fig. 2 (B to E) demonstrated that AVO-treated groups exhibited significant suppression in basal respiration, maximal respiration, and ATP production compared with the control groups, indicating that AVO can effectively inhibit mitochondrial respiration. The metabolic impact of AVO treatment was assessed by plotting extracellular acidification rate (ECAR) and OCR to evaluate shifts in the metabolic state of A-204 cells. AVO treatment elicited a distinct metabolic response. Specifically, A-204 cells transitioned from an energetic state to a quiescent state (fig. S3). Notably, this transition occurred without a significant increase in glycolysis, as evidenced by stable ECAR values and the lack of a shift toward the glycolytic quadrant in the metabolic profile. These results suggest that AVO treatment avoids the excessive glycolytic activation associated with other OXPHOS inhibitors, reducing the risk of lactic acidosis and offering a safer metabolic profile.

AVO has been reported to alleviate tumor hypoxia by primarily inhibiting mitochondrial complex III (*23*, *24*). To investigate whether AVO inhibits complex III in A-204 cells, we generated alternative oxidase (AOX)–expressing A-204 cells by transducing the cells with

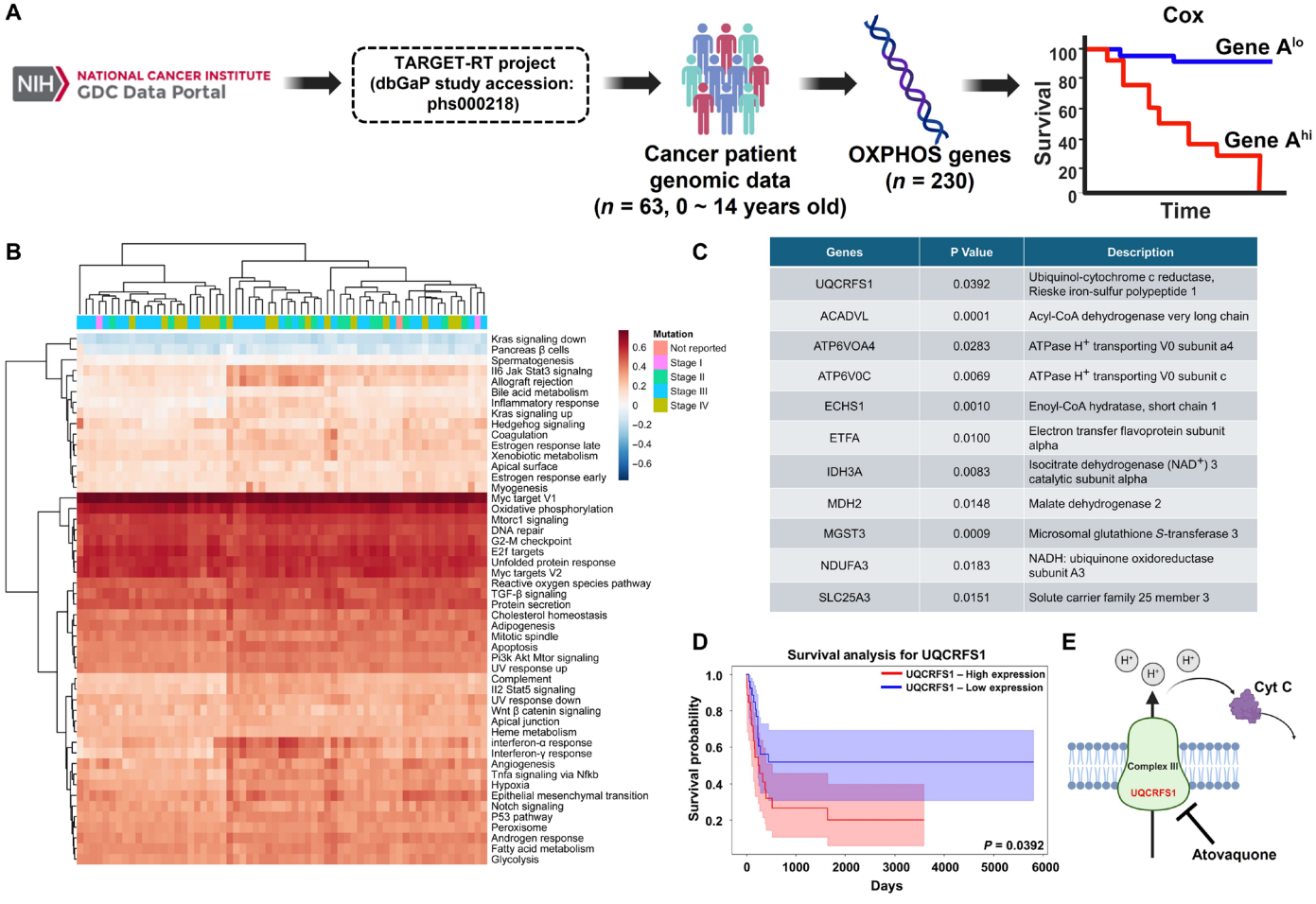

Genes	P Value	Description
UQCRFS1	0.0392	Ubiquinol-cytochrome c reductase, Rieske iron-sulfur polypeptide 1
ACADVL	0.0001	Acyl-CoA dehydrogenase very long chain
ATP6VOA4	0.0283	ATPase H^+ transporting V0 subunit a4
ATP6V0C	0.0069	ATPase H^+ transporting V0 subunit c
ECHS1	0.0010	Enoyl-CoA hydratase, short chain 1
ETFA	0.0100	Electron transfer flavoprotein subunit alpha
IDH3A	0.0083	Isocitrate dehydrogenase (NAD^+) 3 catalytic subunit alpha
MDH2	0.0148	Malate dehydrogenase 2
MGST3	0.0009	Microsomal glutathione *S*-transferase 3
NDUFA3	0.0183	NADH: ubiquinone oxidoreductase subunit A3
SLC25A3	0.0151	Solute carrier family 25 member 3

Fig. 1. OXPHOS up-regulation is a potential metabolic vulnerability in pediatric rhabdoid tumors. (**A**) The scheme of the RNA sequencing, pathway enrichment, and survival curve plotting. (**B**) The heatmap indicated a up-regulation of the OXPHOS pathway across different stages of patients with rhabdoid tumor. TGF-β, transforming growth factor–β; UV, ultraviolet. (**C**) *P* values and description of selected 11 OXPHOS-related genes. ATPase, adenosine triphosphatase; CoA, coenzyme A; NAD^+, nicotinamide adenine dinucleotide (oxidized form); NADH, reduced form of NAD^+. (**D**) Kaplan-Meier survival analysis showed that patients with high UQCRFS1 expression had a significantly worse survival rate compared to those with low expression. (**E**) Schematic showing the UQCRFS1 gene is associated with mitochondrial complex III, inhibited by AVO.

pWPI-AOX–internal ribosomal entry site–green fluorescent protein (GFP) plasmids. GFP-A-204 cells were generated as control. AOX is an auxiliary respiratory enzyme found in plants and other organisms that provides a bypass for the cytochrome segment of mitochondrial complex III when the respiratory chain is impaired (*35*, *36*). We reasoned that AOX will maintain electron flux when complex III is inhibited by AVO, thus rescuing mitochondrial respiration. As shown in fig. S4, AOX-GFP-A-204 cells demonstrated significant OCR recovery in basal respiration ($P < 0.0001$), maximum respiration ($P < 0.0001$), and ATP production ($P = 0.0006$) when treated with AVO when compared to control GFP-A-204 cells that show strong reduction in these parameters. These observations confirm that AVO acts via complex III inhibition to suppress OXPHOS in rhabdoid tumors.

We also compared the performance of AVO with metformin, a commonly applied OXPHOS inhibitor. As seen in fig. S5, the EC_{50} value of metformin for A-204 cells was found to be 13.15 mM, which was significantly higher than that of AVO (~28.36 μM). This confirms that AVO could potentially lead to better therapeutic effects and less off-target toxicity at lower pharmacological concentrations, suggesting improved in vivo performance when compared to metformin.

In vivo OE-MSOT shows that AVO treatment improves tumor oxygenation transiently

We next investigated the in vivo pharmacodynamics of AVO treatment on A-204 xenografts using longitudinal OE-MSOT. OE-MSOT maps tumor oxygenation based on changes in hemoglobin $\%SO_2$ (computed as a ratio of HbO_2 to total hemoglobin) following a switch in delivery from 21% O_2 (medical air) to supplemental (100%) O_2. The ΔsO_2 parameter is computed as the difference between $\%sO_2^{O2}$ and $\%sO_2^{air}$. Compared to static measurements, the dynamic nature of OE-MSOT has been found to provide more robust and reproducible spatiotemporal evaluations of tumor oxygenation (*37*–*39*). We hypothesized that hypoxic tumors will be refractory to hyperoxic gas breathing as high oxygen consumption will increase the oxygen extraction rate, resulting in a reduction of hemoglobin-bound O_2 (HbO_2). Meanwhile, reduction in metabolic oxygen consumption will require a reduction in oxygen extraction, resulting in greater affinity of oxygen for hemoglobin and, hence, higher $\%sO_2^{O2}$

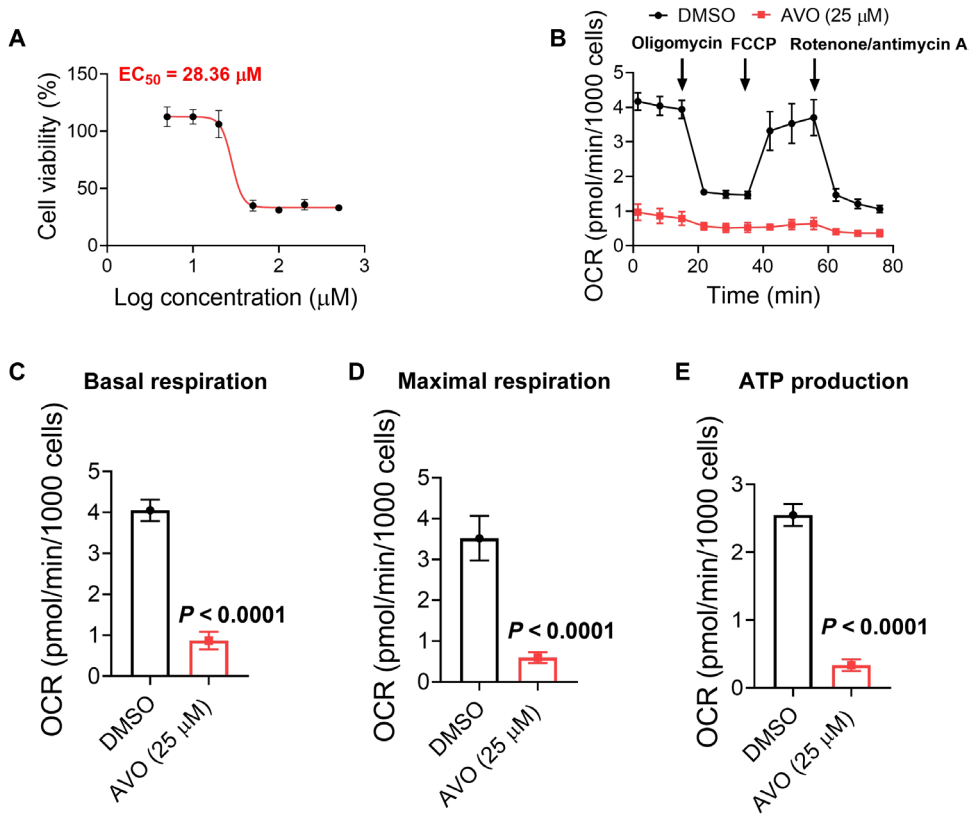

Fig. 2. AVO inhibits mitochondrial respiration of A-204 cells. (**A**) Dose-response curves depicting the effect of AVO on viability of A-204 cells as tested by MTT assay. Seahorse experiment indicating (**B**) OCR traces of A-204 cells treated with vehicle (DMSO) or AVO. (**C** to **E**) Significant reductions in basal respiration, maximal respiration, and ATP production were observed in AVO-treated groups when compared to vehicle-treated controls. All OCR measurements were normalized by Hoechst 33342 staining. Data are presented as means ± SD.

after hyperoxic gas challenge. Thus, blocking mitochondrial function by AVO should lead to reduced O_2 consumption and, hence, higher ΔsO_2.

Application of oxygen gas challenge on tumors at baseline (referred to as day −1, when tumors reached ~50 mm^3) indicated negligible changes in the MSOT derived $\%sO_2$, indicating the hypoxic nature of the tumors (fig. S6). Figure 3 (B and C) shows that AVO-treated tumors depicted a nearly twofold increase in ΔsO_2 from baseline ($\Delta sO_2 = 0.047 \pm 0.02$) to day 3 ($\Delta sO_2 = 0.094 \pm 0.05$) when compared to saline-treated controls ($\Delta sO_2 = 0.050 \pm 0.002$ at day −1 and 0.030 ± 0.011 at day 3). A sharp decline in ΔsO_2 can be seen from day 3 to day 9 in AVO-treated tumors, after AVO treatment was stopped at day 7, indicating a gradual reversion to a hypoxic phenotype. However, a statistically significant difference in ΔsO_2 can still be observed between AVO and saline-treated mice at day 9 ($P = 0.0074$). OE-MSOT at endpoint (day 23 for the AVO-treated group) showed a strong reduction in ΔsO_2 (0.011 ± 0.007), which is comparable to saline-treated controls at endpoint (day 30; 0.016 ± 0.011). This decrease in ΔsO_2 can be related to continued tumor growth after cessation of therapy, at indicated by increase in tumor volume. Increased pimonidazole immunofluorescence (Fig. 4, A and B, and fig. S7) validated our in vivo OE-MSOT observations.

Our results highlight the importance of longitudinal monitoring of hypoxia modulation by AVO using OE-MSOT. As the duration of hypoxia alleviation by AVO is short-lived and wanes off after the treatment is stopped, it is imperative that combination with radiotherapy is timed appropriately, so that the tumors are irradiated when they are most oxygenated. After establishing the oxygenation dynamics, a separate cohort of AVO-treated tumor-bearing mice was subjected to a single low 10-Gy dose of focused x-ray, 1 day after AVO treatment was stopped. Ex vivo pimonidazole staining confirmed the well-oxygenated status of tumors at day 8 [Fig. 4, A and D (a)]. Immediate (day 9) and longer-term changes in tumor oxygenation following AVO and 10 Gy combination treatment were assessed with OE-MSOT and immunofluorescence and compared to mice receiving 10-Gy irradiation only. As seen in Fig. 3 (E and F), irradiation of AVO-treated tumors results in an immediate and strong decrease in ΔsO_2 (0.044 ± 0.002) at day 9 compared to ΔsO_2 (0.142 ± 0.021) at day 3 ($P = 0.0013$), presumably caused by enhanced cellular death. We hypothesized that increased oxygenation by AVO bolstered greater reactive oxygen species–mediated cell killing by low-dose radiation. We observed a slight increase in tumor oxygenation a few days after irradiation, as measured by both OE-MSOT and pimonidazole immunostaining [Fig. 4, B and D (b), and fig. S7]. It is reasonable to assume that increased cellular apoptosis resulted in reduced oxygen consumption and hence a temporary increase in intratumoral oxygen levels. Ki-67 staining and hematoxylin and eosin (H&E) on day 12 validated our premise [Fig. 4, C and D (c)]. To confirm that hypoxia modulation by AVO was tumor specific and to confirm that pimonidazole staining truly reflected tissue oxygenation, we assessed major

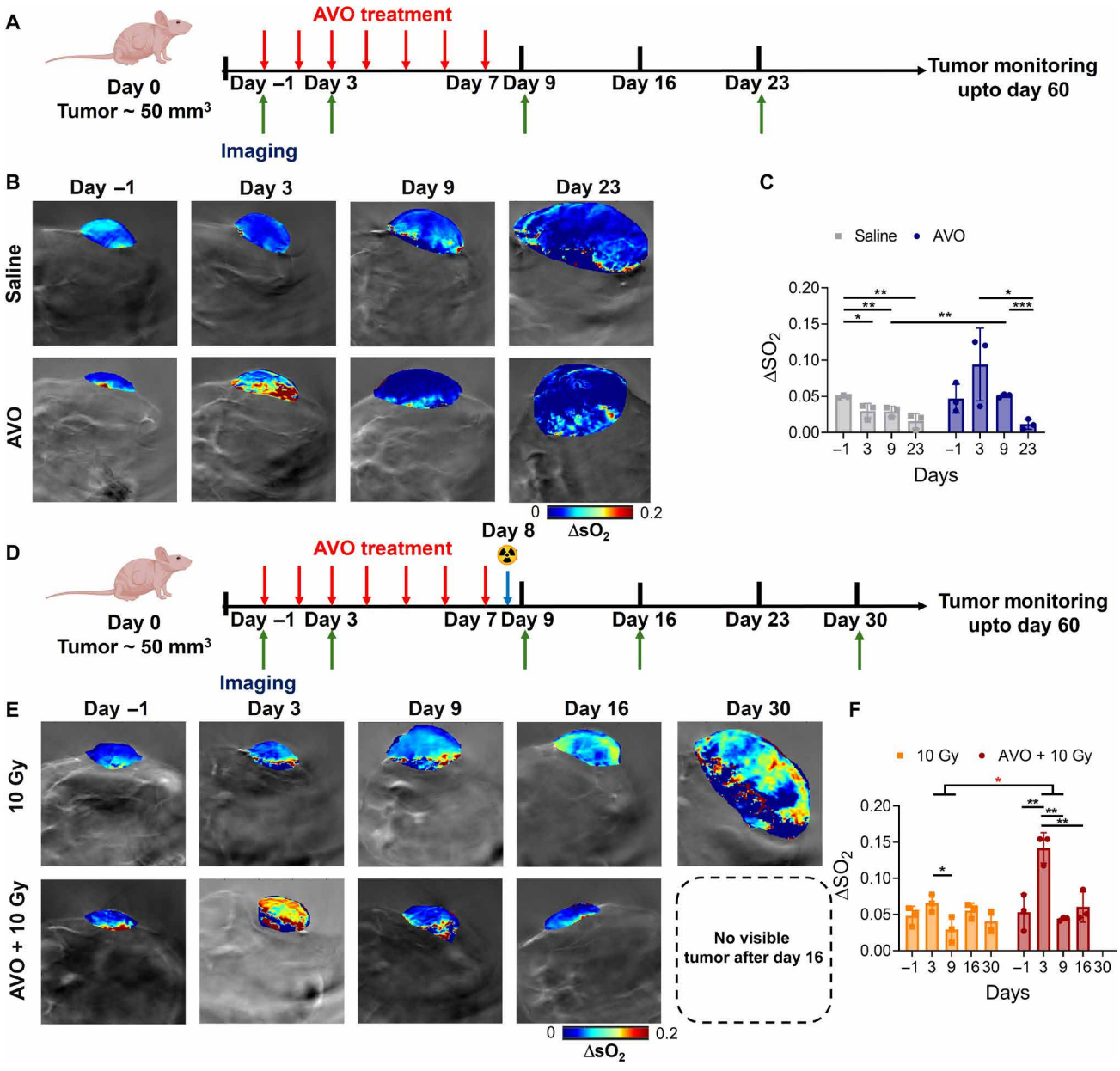

Fig. 3. OE-MSOT shows that AVO treatment improves tumor oxygenation transiently on A-204 xenografts. (**A**) Treatment and imaging timeline for the saline- or AVO-treated groups ($n = 3$). (**B**) Parametric maps and (**C**) quantitative analysis of tumor ΔsO_2 of saline and AVO treatment groups at each time point. (**D**) Treatment and imaging timeline for the 10 Gy– or AVO and 10 Gy–treated groups ($n = 3$). (**E**) Parametric maps and (**F**) quantification analysis of tumor ΔsO_2 of the 10 Gy and AVO and 10 Gy treatment groups at each time point. Data are presented as means ± SD. Statistical analysis as indicated.

organs (heart, liver, kidney, and muscle) in the saline- and AVO and 10 Gy–treated groups. As seen in fig. S8, no apparent difference was observed in pimonidazole staining for any of the tissues between saline and the combination treatment groups.

In contrast, tumors treated with irradiation only remained uniformly hypoxic with no significant changes in ΔsO_2 values, consistent with resistance to low-dose radiotherapy (Fig. 3, E and F). Pimonidazole staining of irradiated tumors on day 9 and endpoint indicated similar hypoxia levels as the saline-treated groups (Fig. 4, A and B), which further corroborated our observations in vivo. Together, our data indicate the potential utility of monitoring oxygenation by OE-MSOT and ΔsO_2 as a noninvasive biomarker to predict and evaluate tumor response to hypoxia modulating therapies and radiotherapy. As MSOT involves light and ultrasound for noninvasive interrogation of tissues, we believe that it could be an attractive modality for imaging-based treatment planning and evaluation in children with cancers.

AVO enhances the sensitivity of A-204 tumors to low-dose RT

Given the significant improvement in tumor oxygenation after AVO treatment observed by OE-MSOT and pimonidazole staining, we hypothesized that AVO could enhance the sensitivity of A-204 tumors

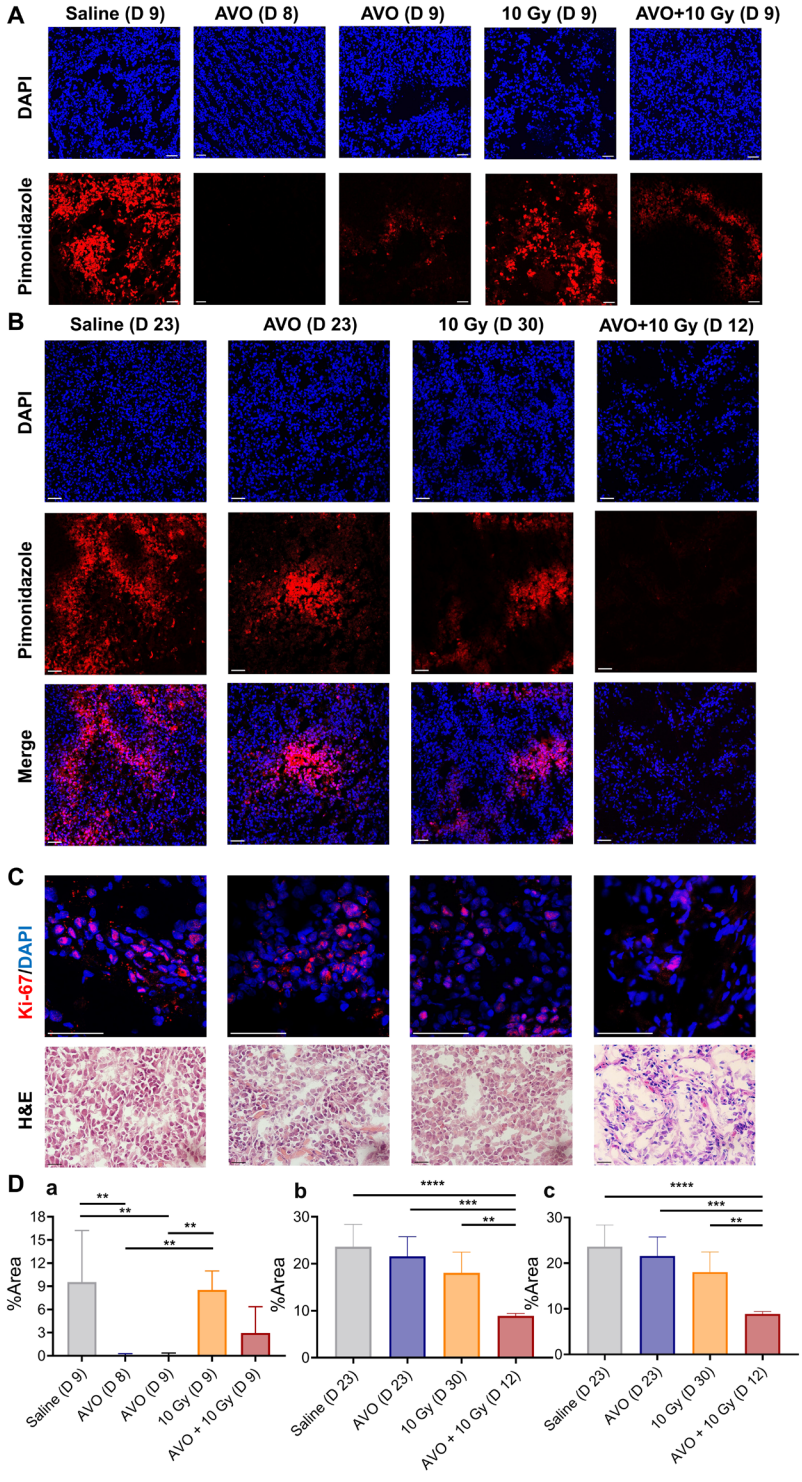

Fig. 4. Immunofluorescence imaging shows that AVO alleviates tumor hypoxia. Immunofluorescence imaging of pimonidazole staining of tumors harvested at days 8 and 9 (mid-treatment) (**A**) and endpoint (**B**) for different treatment groups. (**C**) Ki-67 and hematoxylin and eosin (H&E) staining at endpoint for different groups. Scale bars, 50 μm. (**D**) Quantitative analysis of pimonidazole at (a) day 9 and (b) end point and Ki-67 at endpoint (c) in all treatment groups. Data are presented as means ± SD. DAPI, 4′,6-diamidino-2-phenylindole; D, day.

to low-dose RT and improve tumor responses. Thus, after imaging, mice in monotherapy and combination therapy groups were monitored for tumor growth and survival over 60 days (Fig. 5A). Mouse body weight was also measured, as weight changes serve as a valuable parameter for assessing treatment toxicity in vivo (*40*). As shown in Fig. 5B, the body weight curves exhibited no significant difference among all treatment groups, suggesting that AVO, 10 Gy, or combined treatments did not cause noticeable systemic toxic effects on mice, compared to saline-treated controls. Tumor volume changes (Fig. 5C) showed that the average time required for tumors to reach 1000 mm^3 was 29 days for the saline-treated group, 30 days for the AVO-treated group, and 42 days for the 10 Gy–treated group. One tumor in the RT only group had excellent response. However, for the AVO and 10 Gy–treated group, all the tumors were completely abolished within 10 days posttreatment, and, most notably, tumors did not recur for the remainder of the study. Endpoint tumor volume changes as measured by calipers (Fig. 5D) or observed visually (fig. S9 and Fig. 5E) demonstrated significant abrogation in all mice treated with AVO and 10 Gy when compared to monotherapy or saline-treated mice ($P < 0.0001$). As expected, the stellar tumor inhibitory effects of AVO and RT combination therapy, coupled with minimal toxicity resulted in significantly extended animal survival (Fig. 5F).

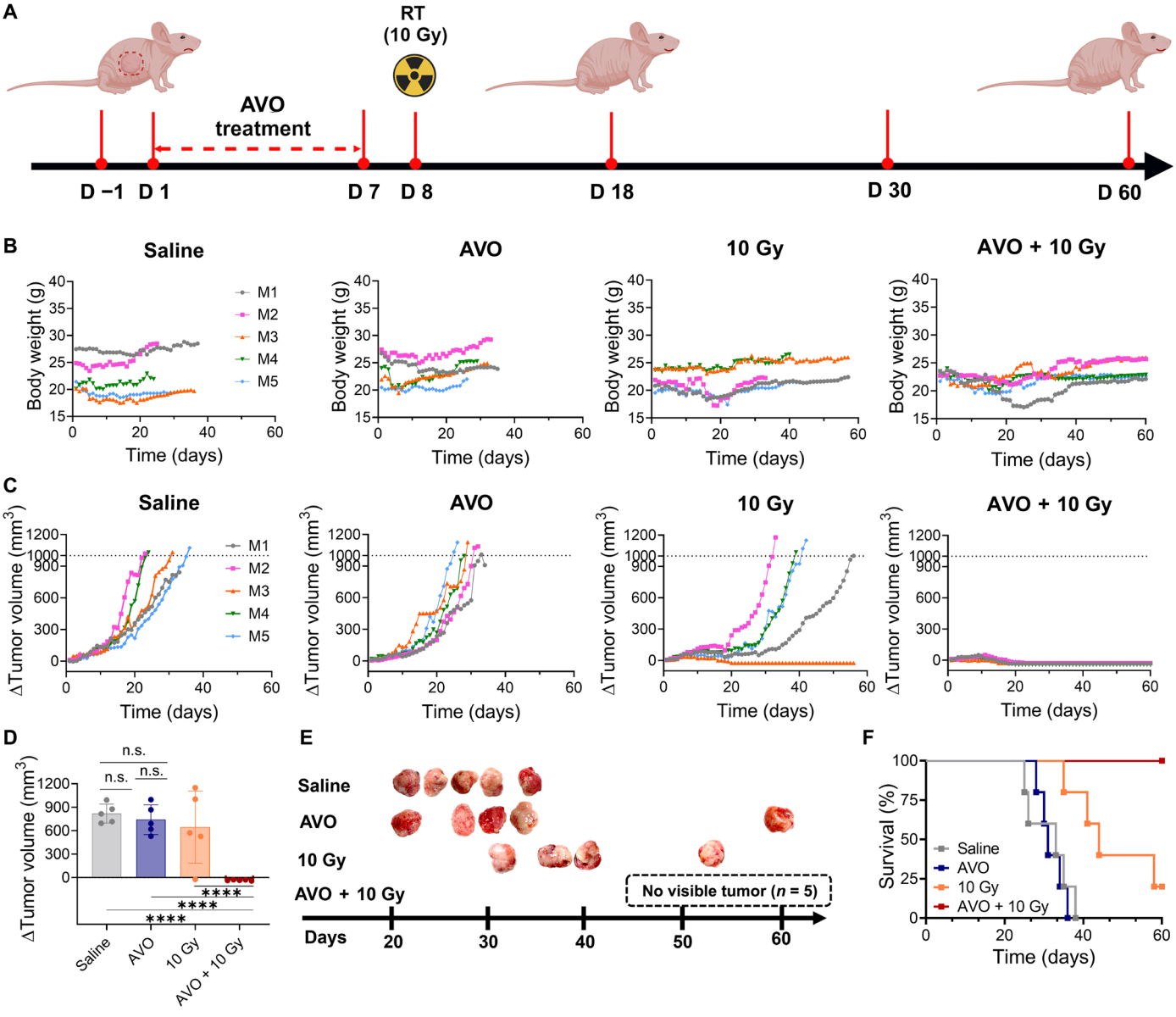

Fig. 5. AVO increases low-dose radiation treatment response in A-204 xenografts. (**A**) Treatment scheme of the AVO and 10 Gy combination therapy group. Graphs depicting (**B**) body weight and (**C**) tumor volume changes over 60 days in all treatment groups ($n = 5$). ΔTumor volume was computed by subtracting tumor volumes at baseline from the tumor volume at each time point. (**D**) ΔTumor volumes and (**E**) photographs of excised tumors at endpoint for all groups. No visible tumors were found in the AVO and 10 Gy–treated groups on day 60. n.s., not significant. (**F**) Kaplan-Meier survival curves for all treatment groups. Data are presented as means ± SD. Statistical analysis as indicated in Materials and Methods.

We used γ-H2AX as a biomarker of DNA damage to evaluate irradiation response in A-204 tumors (*41*). As seen in Fig. 6 (A and B), AVO and 10 Gy–treated tumors depicted more obvious γ-H2AX signal when compared to the saline-treated ($P = 0.0038$), AVO-treated ($P = 0.0011$), and 10 Gy–treated groups [$P = 0.0284$; Fig. 6C (b)], demonstrating the radiosensitizing effect of AVO on typically radioresistant tumors. Subsequently, H&E staining of other organs including the heart, liver, kidney, and muscle was performed to further evaluate the treatment toxicity. As shown in Fig. 6D, no detectable necrosis or morphological changes were observed in these organs, which is consistent with the conclusions drawn from the body weight results.

To test whether increased radiation doses would elicit tumor inhibitory effects, a separate cohort of A-204–xenografted mice were treated with 30-Gy dose (fractionated over 5 days, 6 Gy per fraction). Another group of mice was treated with AVO and fractionated RT dose (treatment schema shown in fig. S10). As seen in fig. S10A, a fractionated 30-Gy dose was well tolerated (no apparent change in body weight) but only succeeded in slowing the tumor growth. In one mouse, the tumor did not respond to irradiation, as indicated by the exponential increase in tumor volume. On the other hand, when combined with AVO, a 30-Gy fractionated dose exerted notable tumor control, with tumors disappearing within 5 days of stopping treatment (fig. S10B).

Together, the data demonstrate that, although AVO does not exert therapeutic effect as a monotherapy for MRT, the combination of AVO and low-dose RT can be an effective and efficient strategy to maximize responses, with potential for clinical application in MRT treatment in the future. Our findings are important for children with MRT through two avenues. First, we demonstrate that AVO can serve as a safe, FDA-approved adjuvant to markedly enhance therapeutic efficacy of radiotherapy in otherwise radioresistant tumors and increase overall recurrence-free survival. Second, the ability to obliterate tumors at low radiation doses serves to greatly assuage concerns about longer-term radiotoxicities or secondary tumor growth, which are known to affect quality of life and survival in patients subjected to aggressive chemoradiation therapies, earlier in childhood.

DCE-MSOT indicates that AVO-mediated reduction in tumor hypoxia does not depend on vascular normalization

Prolonged hypoxia could result from irregular tumor vascularization in aggressive solid tumors (*42*), which compromises tumor perfusion and hinders effective oxygen delivery (*43*). To investigate whether AVO treatment could relieve tumoral hypoxia by vascular normalization, we used DCE-MSOT to visualize and quantify changes in tumor vascular perfusion. Figure 7A displays the parametric maps of normalized wash-in rate (NK^{trans}) and washout rate (K_{ep}) of ICG for the saline and AVO-treated groups on day −1 (baseline), and days 3, 9, and 23. There were no significant differences detected in NK^{trans} and K_{ep} values before, during, and after AVO treatment (Fig. 7B). Kinetic curves plotted for ICG accumulation over 15 min of dynamic scan demonstrated no apparent differences between tumors treated with saline or AVO (Fig. 7C). These results, together with our in vitro bioenergetics stress test, in vivo OE-MSOT and ex vivo histopathological data establish that improved tumor oxygenation by AVO is mediated by associated reduction in metabolic demand for oxygen and not through vascular normalization. Furthermore, we also compared the parametric maps, NK^{trans} and K_{ep} values, and ICG signal kinetics in the tumors were subjected to 10-Gy monotherapy and AVO and 10 Gy combination treatment groups. The results of fig. S11 (A and B) indicate that no meaningful difference was observed between the different groups. Although changes in vascular perfusion are commonly observed after RT in solid tumors, we did not find any notable alterations in our study, possibly attributed to the intrinsic radioresistance of MRT to low-dose radiation.

Immunofluorescence imaging of CD31 was subsequently conducted on excised tumor tissues at day 9 (fig. S11C) and endpoint (fig. S12) to validate our in vivo findings. Consistent with the DCE-MSOT results, CD31 staining did not show any marked difference among different treatment groups, confirming that AVO had no impact on vessel structure or functionality.

OE-MSOT can distinguish between AVO-sensitive and AVO-resistant A-204 xenografts

To confirm that AVO was essential for the observed therapeutic efficacy of low-dose RT, we developed AVO-resistant A-204 cell line (A^R-A-204) by treating cells to escalating doses of AVO over time (Fig. 8A). OCR and ECAR traces were first assessed in A^R-A-204 cells to establish baseline. The results shown in Fig. 8B indicated that continuous AVO treatment resulted in lower baseline levels of mitochondrial respiration in A^R-A-204 cells, significantly reducing basal respiration, maximal respiration, and ATP production ($P < 0.0001$; Fig. 8, D to F) when compared to naïve A-204 cells. While ECAR traces showed no significant differences in aerobic glycolysis between A-204 and A^R-A-204 cells (Fig. 8C), marked increase in glycolytic capacity ($P = 0.0002$) and glycolytic reserve ($P < 0.0001$; fig. S13) were observed alongside a metabolic shift to a quiescent state in A^R-A-204 cells. Our results indicate that metabolic plasticity associated with treatment resistance in MRT and warrant further examination into the metabolic effects of AVO.

Next, A^R-A-204 xenografts were treated with saline or AVO followed by 10-Gy x-ray, and tumor oxygenation was monitored longitudinally using OE-MSOT. As seen in Fig. 8 (G and H), saline-treated A^R-A-204 tumor exhibited higher oxygenation levels at all time points ($\Delta sO_2 = 0.048 \pm 0.01$ at day 3, $\Delta sO_2 = 0.035 \pm 0.01$ at day 9, and $\Delta sO_2 = 0.027 \pm 0.003$ at day 23) when compared to saline-treated A-204 tumors (Fig. 3C; $\Delta sO_2 = 0.030 \pm 0.011$ at day 3, $\Delta sO_2 = 0.030 \pm 0.007$ at day 9, and $\Delta sO_2 = 0.016 \pm 0.01$ at day 23). This finding suggests that constitutive down-regulation of OXPHOS in A^R-A-204 results in less severe hypoxic microenvironment in MRT. Lower pimonidazole immunofluorescence signals (Fig. 8, I and J) validated our in vivo OE-MSOT observations. These encouraging data indicate the potential of ΔsO_2 to serve as an imaging biomarker of treatment resistance to metabolic modulatory therapies.

Further, in the AVO and 10 Gy–treated A^R-A-204 xenografts (Fig. 8, G and H), OE-MSOT at midpoint revealed no difference from saline-treated groups and a significant decrease in ΔsO_2 (day 3; 0.042 ± 0.01), contrasting with the A-204 xenografts (Fig. 3E; day 3; 0.142 ± 0.02), which confirms that A^R-A-204 xenografts no longer respond to AVO treatment and that hypoxia alleviation seen in wild-type A-204 tumors was solely reliant on AVO-mediated OXPHOS inhibition. Pimonidazole exhibited an obvious higher signal in the AVO and 10 Gy group (Fig. 8I) compared to the wild-type A-204 combination treatment group, further supporting our OE-MSOT observations.

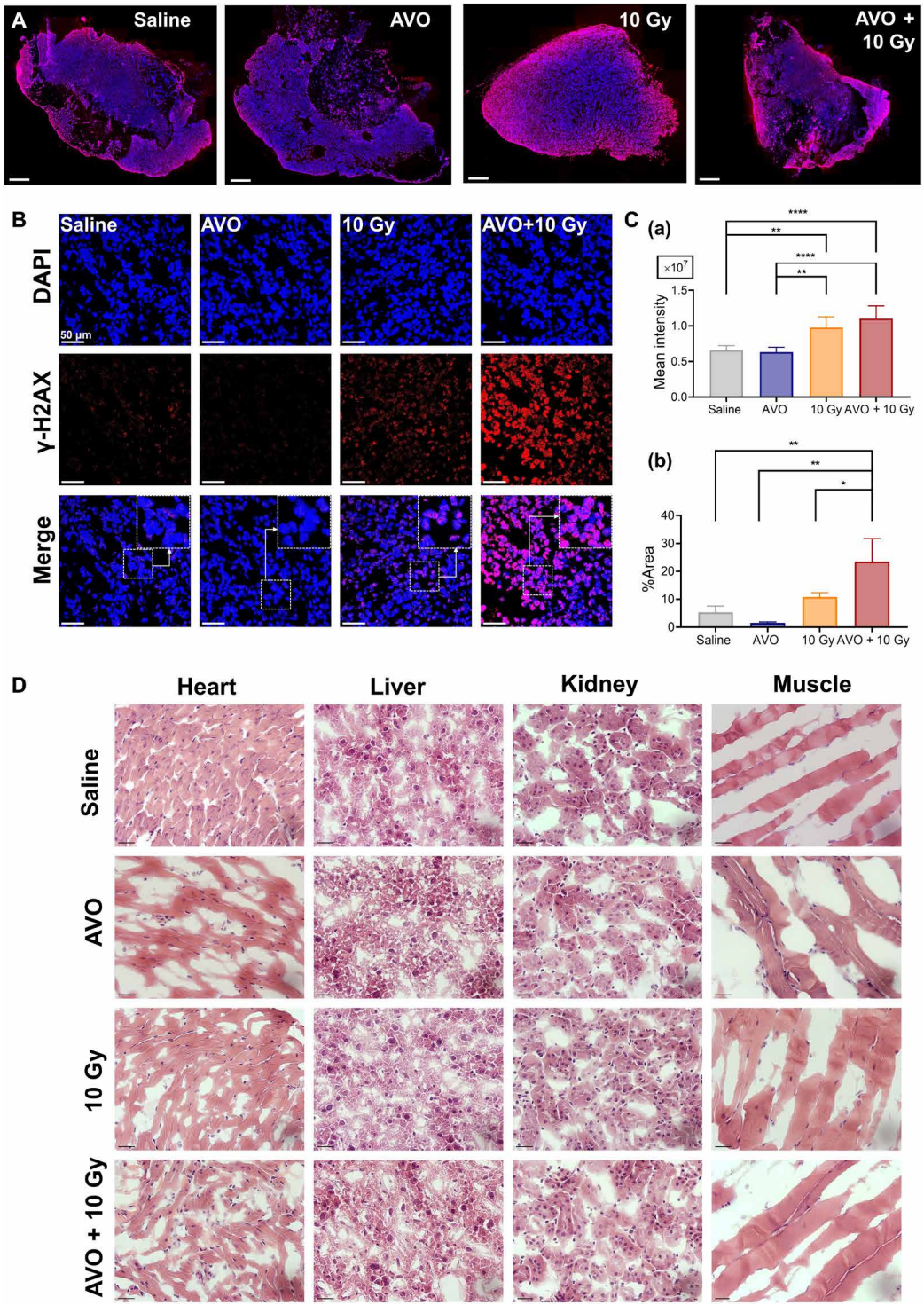

Fig. 6. AVO enhanced DNA damage caused by RT. (**A**) Whole-tissue imaging and (**B**) confocal micrographs of γ-H2AX immunofluorescence staining of all treatment groups on Day 9. Insets: Stained A-204 tissue at high magnification. Scale bars, 50 μm for confocal images and 1000 μm for whole tumor sections. (**C**) Quantification of γ-H2AX staining in whole tumor sections (a) and confocal micrographs (b) of all treatment groups. (**D**) H&E staining for the heart, liver, kidney, and muscle from various treatment groups. Scale bars, 100 μm. Data represented as means ± SD.

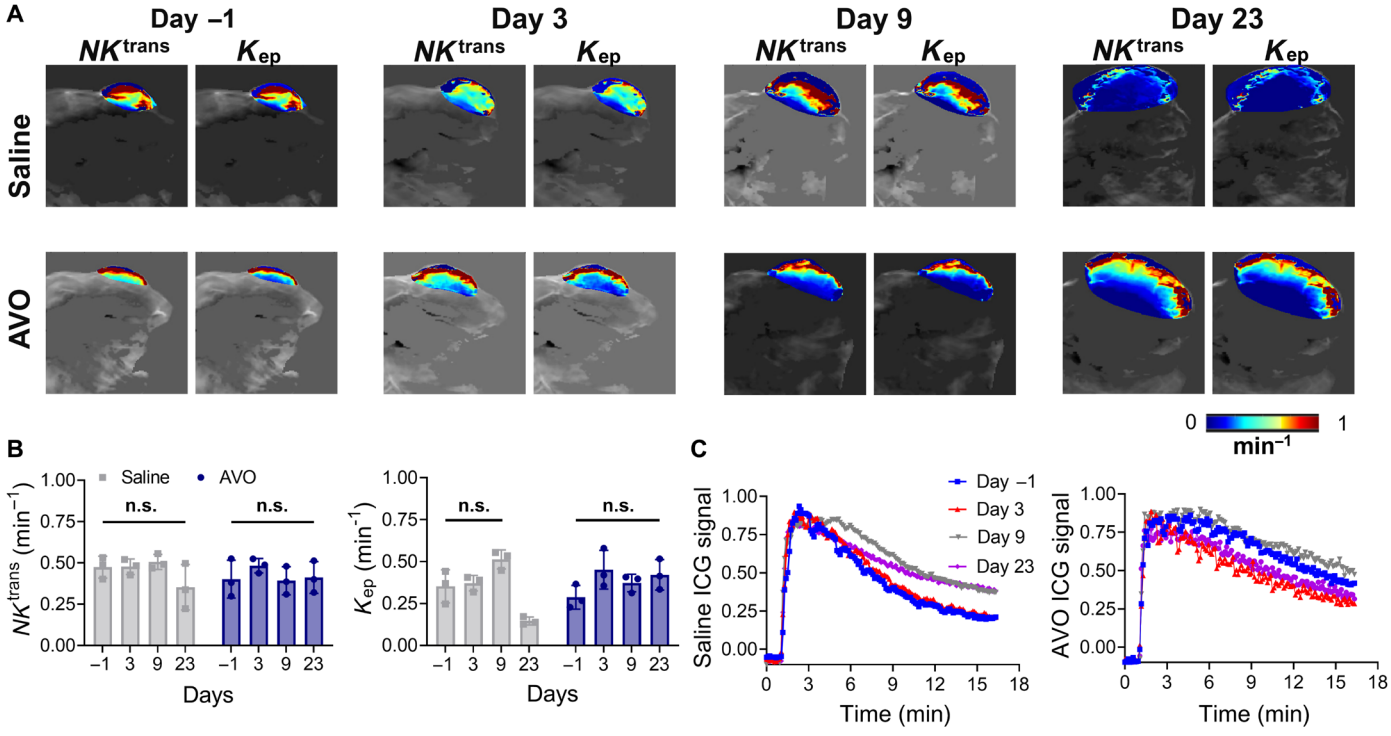

Fig. 7. DCE-MSOT shows that AVO has no impact on tumor perfusion. (**A**) Parametric maps and (**B**) quantification analysis of NK^{trans} and K_{ep} for the saline- and AVO-treated A-204 xenografts on days −1, 3, 9, and 23 ($n = 3$) (**C**) Kinetic curves depicting ICG accumulation in tumors over time in saline and AVO treatment groups. Data presented as means ± SD.

AVO-resistant A-204 xenografts do not respond to AVO-sensitized radiotherapy

Because AVO treatment did not alleviate hypoxia in the A^R-A-204 xenografts, we further investigated and validated whether the treatment response of AVO and 10 Gy would also be diminished in these tumors. As shown in Fig. 9A, there was no notable fluctuation in body weight, except for one mouse in the AVO and 10 Gy–treated group, which experienced around 25% weight reduction relative to baseline immediately after receiving 10-Gy irradiation. Therefore, this mouse was excluded in the subsequent study. The survival rates and tumor volume changes (Fig. 9, B and C) showed that the average time required for tumors to reach 1000 mm^3 was 40 days for the saline-treated group. The tumor growth was markedly slower compared to the 29 days (to reach endpoint) observed in saline-treated naïve A-204 tumors, suggesting that OXPHOS down-regulation could make MRT less aggressive. Mice treated with AVO and 10 Gy combination treatment took an average of 54 days to reach 1000 mm^3. Although the tumor volume showed a slight reduction after the treatment on day 9, the tumor continued to grow in the following weeks, indicating that A^R-A-204 tumors did not benefit from the therapy (Fig. 9, C and D). Our data suggest that, as expected, AVO no longer exerted a radiosensitizing effect in drug-resistant xenografts. Last, as shown in Fig. 9E, H&E staining showed no toxicity observed in the normal organs including the heart, liver, kidney, and muscle, and no detectable morphological changes or apparent necrosis was observed in the tumors excised from either saline or combination therapy cohorts.

Mathematical modeling reveals a synergistic relationship between AVO and radiotherapy

A mathematical framework was built to elucidate the dynamic interplay between tumor growth, radiotherapy, and hypoxia alleviation with AVO in MRT. The model was calibrated by fitting it to individual mouse tumor growth kinetics under different treatment conditions. The parameter estimates derived via nonlinear least squares fitting are presented in table S1. As shown in Fig. 10A, tumor growth kinetics under AVO monotherapy closely resemble those of untreated controls. The estimated tumor growth rate parameter (γ) remained effectively unchanged between control and AVO-only conditions (table S1), reinforcing the conclusion that AVO alone did not inhibit tumor progression. When combined with single 10-Gy dose, AVO produced a more pronounced reduction in tumor growth than radiation alone, confirming its role as a radiosensitizer. A strong Pearson correlation between modeled and observed tumor volumes (fig. S14) supported the accuracy and robustness of the model fits.

Figure S15 further validates the accuracy of the model in capturing tumor growth dynamics across all treatment groups by comparing virtual cohort predictions (solid lines with shaded confidence intervals) to experimental tumor volume data (blue points). This comparison shows strong agreement under control, AVO monotherapy, radiation monotherapy, and combination therapy conditions, with significant correlations ($P < 0.001$) in all cases. Notably, the virtual cohort effectively captures both the mean tumor growth trajectory, and the variability observed experimentally, underscoring the reliability of the model in mimicking preclinical outcomes.

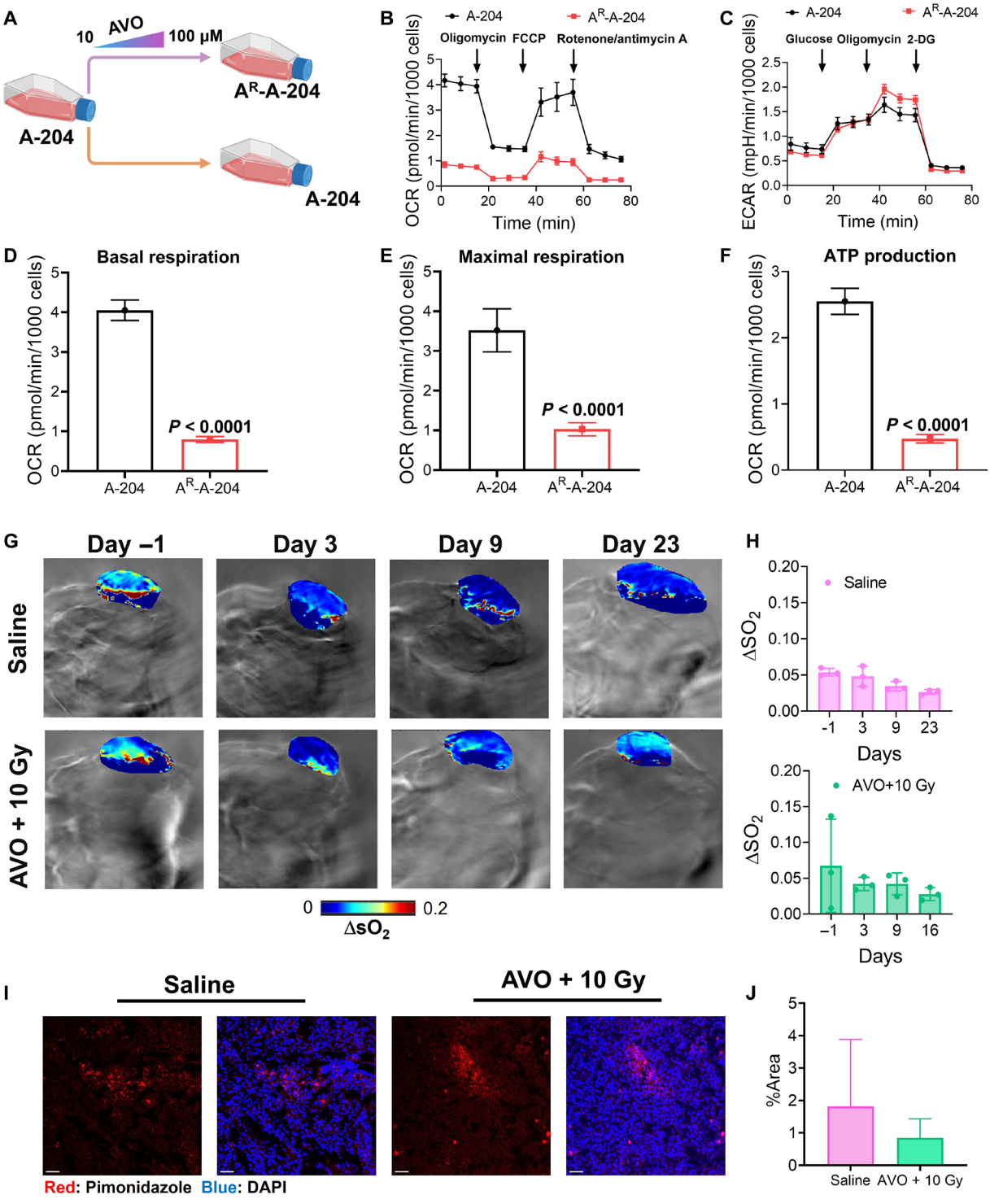

Fig. 8. AVO resistant A^R-A-204 tumors depict altered metabolism and intratumoral hypoxia. (**A**) Scheme depicting the generation of AVO-resistant (A^R-A-204) cells. (**B**) OCR and (**C**) ECAR traces of wild-type A-204 and A^R-A-204 cells. (**D** to **F**) Statistically significant reductions in basal respiration, maximal respiration, and ATP production as observed in A^R-A-204 cells when compared to wild-type A-204 cells. (**G**) Parametric maps and (**H**) quantitative analysis of tumor ΔsO_2 for the saline- and AVO and 10 Gy–treated A^R-A-204 xenografts on days −1, 3, 9, and 23 ($n = 3$). (**I**) Confocal imaging and (**J**) quantitative analysis of pimonidazole staining of excised saline- and AVO and 10 Gy–treated tumors at endpoint. Scale bars, 50 μm.

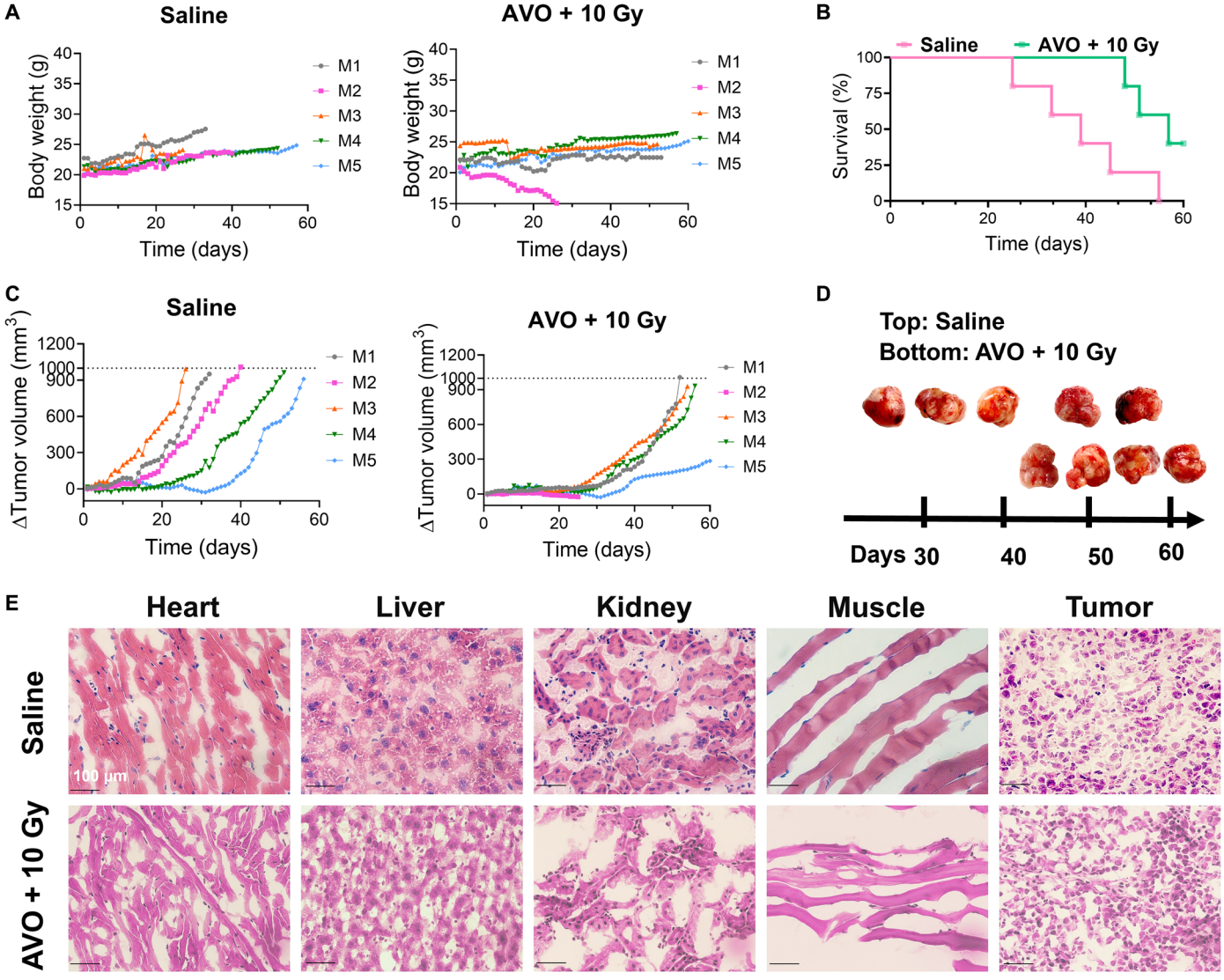

Fig. 9. A^{R}-A-204 xenografts do not respond to combination therapy. (**A**) Body weight curves of the saline- and AVO and 10 Gy–treated groups. (**B**) Kaplan-Meier survival curves and (**C**) individual tumor growth curves depicting change in tumor volume from baseline for both groups. (**D**) Photographs of excised tumors taken at endpoint ($n = 5$). (**E**) H&E staining of the heart, liver, kidney, muscle, and tumor tissues of each treamtment groups. Scale bars, 100 μm.

These virtual animal cohorts were generated to validate the methodology used for simulating tumor dynamics in human cohorts, ensuring the robustness of the approach before its translation to first-in-human settings.

Tumor static exposure (TSE) curve analysis that quantifies the relationship between AVO dose and the corresponding RT dose required to maintain tumor stasis in mice, as obtained from Eq. 1, is presented in Fig. 10B. Mathematically, stasis occurs when tumor growth is exactly balanced by treatment-induced cell death, resulting in no net change in tumor volume over time $\left(\frac{dV(t)}{dt} = 0\right)$ (*44*–*46*). The TSE curve exhibits a concave-up shape, indicating that the reduction in radiation dose requirements accelerates with increasing AVO doses, particularly in the lower dose range, reflecting a synergistic interaction between AVO and radiation, where AVO enhances radiosensitivity by alleviating hypoxia. At higher AVO doses, the curve begins to flatten, reflecting saturation of this synergistic effect. Above the TSE curve, the shaded green region represents combinations of AVO and radiation doses that not only maintain stasis but also drive tumors into regression. Conversely, dose combinations below the curve are insufficient to counteract tumor growth, resulting in continued expansion of tumor volume. Thus, while the curve itself delineates the boundary between stable and growing tumors, the shaded area highlights the potential for more aggressive tumor shrinkage when both AVO and radiation doses are combined effectively. These findings reinforce the value of AVO as a radiosensitizer and provide actionable insights into dose levels that can shift the treatment goal from stabilization to active tumor shrinkage.

Translational modeling predicts efficacy of the combination treatment in first-in-human settings

To assess the clinical efficacy of our combination treatment, we applied the mathematical model to a virtual patient cohort to predict

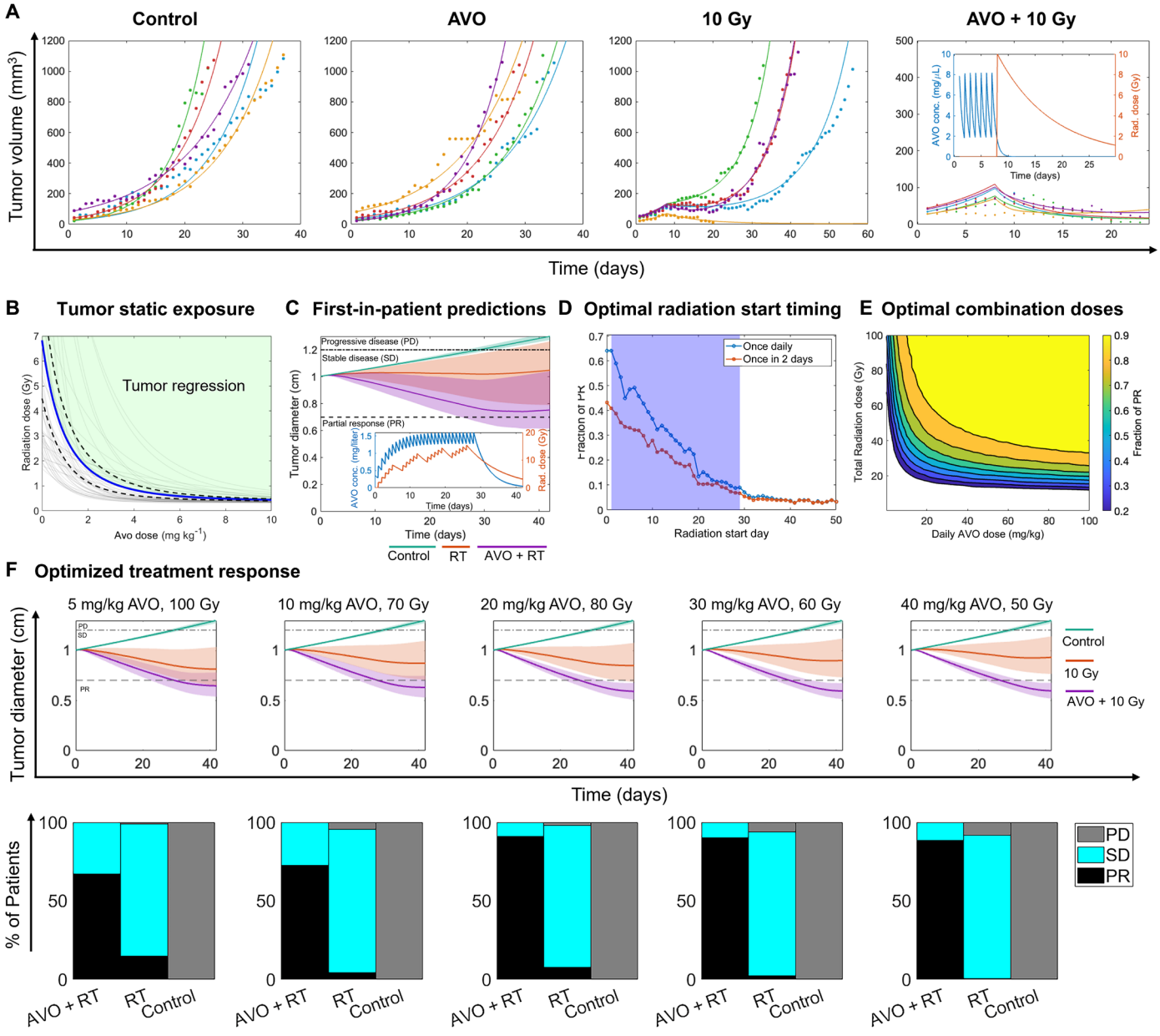

Fig. 10. Mathematical modeling predicts efficacy of optimized combination treatment in virtual patient cohort. (**A**) Model fits to mouse tumor growth kinetics under different therapeutic regimens. The inset in AVO and RT graph shows the modeled AVO concentration kinetics (left *y* axis) and the modeled biological dissipation of a single radiation dose (right *y* axis). (**B**) Tumor static exposure (TSE) curve (blue) illustrating how increasing AVO dose reduces the radiation dose required for tumor stasis; 95% confidence interval around the TSE curve is shown with dashed black lines; the green area above the curve indicates doses that lead to tumor regression. (**C**) First-in-patient simulations using a regimen of AVO (10 mg/kg per day for 4 weeks) and fractionated radiation (2 Gy per fraction, 5 days/week for 4 weeks) show mean tumor trajectories (solid lines) with shaded 95% confidence intervals for different groups in virtual patients. Horizontal dashed and dotted-dashed lines mark thresholds delineating partial response (PR), stable disease (SD), and progressive disease (PD). The inset in (C) displays AVO concentration (left *y* axis) and radiation effects (right *y* axis) over the extended, fractionated schedule. (**D**) Radiation start time optimization relative to the 4-week AVO schedule (blue band) illustrates how adjusting radiation initiation affects the fraction of patients achieving PR. Simulations included daily AVO administration and an alternate schedule of once every 2 days to evaluate the effect of dosing frequency on timing optimization. (**E**) Combination dose optimization contour plot shows PR fractions across AVO and total radiation doses, identifying clinically relevant dose pairs that improve efficacy while reducing radiation exposure. (**F**) Optimized treatment responses at selected AVO/radiation dose combinations: Top panels show mean tumor trajectories (solid lines) with 95% confidence intervals for control, radiation-only, and AVO and RT. Bottom panels present bar plots of treatment outcome distributions (PR, SD, and PD) within the virtual patient cohort.

tumor response in a first-in-patient setting (Fig. 10C). Parameter values were extrapolated from preclinical mouse data to humans using allometric scaling, while population variability was captured through a virtual patient cohort of 500 individuals. The simulations evaluated tumor dynamics under three treatment conditions: control, radiation-only (2 Gy per fraction, 5 days/week for 4 weeks), and AVO and radiation (AVO at 10 mg/kg per day for 4 weeks combined with the same radiation schedule). Mean tumor trajectories (solid lines) and 95% confidence intervals (shaded regions) are shown to represent population-level variability in response. Thresholds for progressive disease (PD), stable disease (SD), and partial response (PR), as defined by the clinical gold standard RECIST 1.1 criteria, were delineated by horizontal dashed and dotted-dashed lines. These thresholds directly link the simulated tumor diameter changes to clinical oncology endpoints, enabling the translation of model predictions into meaningful clinical outcomes. The inset in Fig. 10C provides additional context, displaying the pharmacokinetic profile of AVO (left *y* axis) and the cumulative biological effects of fractionated radiation (right *y* axis) over the 4-week treatment schedule.

The results reveal that untreated tumors exhibit continuous growth, while radiation monotherapy slows tumor progression. In contrast, combination therapy leads to significant tumor shrinkage, demonstrating the radiosensitizing effect of AVO. Of note, the doses used in this numerical experiment were chosen on the basis of the existing clinical regimens for other indications and tumor types, rather than being optimized specifically for the context modeled here. This raises the possibility that better outcomes could be achieved through careful optimization of AVO and radiation doses. Accordingly, we undertook a series of optimization experiments.

To assess the impact of irradiation start timing relative to AVO and the administration frequency of AVO on treatment outcomes, simulations were performed for radiation initiation days ranging from day 0 (simultaneous with AVO start) to day 30 (radiation starting 30 days after AVO initiation). AVO was administered at a dose of 10 mg/kg either daily or once every 2 days for 4 weeks, while radiation was delivered at 2 Gy per fraction, 5 days per week, for 4 weeks. Figure 10D demonstrates that daily AVO administration leads to higher PR rates across all start times compared to the alternate once-every-2-days schedule. The highest PR rates are observed when radiation is initiated concurrently with or shortly after the start of AVO treatment, emphasizing the importance of synchronizing radiation delivery with the radiosensitization effects of AVO. Delaying radiation initiation within the 4-week AVO treatment window results in a steep decline in PR rates. Beyond the 4-week AVO treatment period, PR rates plateau at persistently low levels, reflecting the diminished radiosensitization effect once AVO administration ends. These findings highlight the necessity of maintaining consistent AVO plasma concentrations and synchronizing radiation timing during the active treatment phase to maximize the synergistic effects of the combination therapy.

Further, Fig. 10E explores the synergistic effects of AVO and radiation dose combinations by simulating 2500 dose pairs (50 values each for AVO and radiation doses) and calculating the fraction of patients achieving PR for each combination. AVO doses ranged from 0.1 to 100 mg/kg per day, while total radiation doses ranged from 0.1 to 100 Gy (administered as fractionated doses over 4 weeks). The resulting contour plot demonstrates that higher AVO doses significantly reduce the radiation required to achieve PR in a substantial proportion of the virtual patient cohort, underscoring the synergistic interplay between the two modalities. Notably, in corroboration with the TSE analysis, diminishing returns at very high AVO doses were observed, as reflected in the large horizontal spread of the yellow region, where further increases in AVO provide minimal incremental benefit in reducing radiation requirements.

Last, we evaluated the impact of optimized treatment regimens on tumor outcomes in the virtual patient cohort. The five regimens analyzed were selected from the contour plot (Fig. 10F) to represent diverse combinations of AVO and radiation doses, spanning low AVO with high radiation [e.g., AVO (5 mg/kg) and 100 Gy] to high AVO with low radiation [e.g., AVO (40 mg/kg) and 50 Gy]. The top row of Fig. 10F presents mean tumor trajectories (solid lines) with 95% confidence intervals (shaded regions) under each regimen, alongside control and radiation-only treatments. The bottom row displays the corresponding outcome distributions as bar plots, categorizing the percentage of patients achieving PR, SD, or PD. A clear enhancement in treatment efficacy as AVO doses increase and RT doses decrease across the selected regimens can be seen. Lower-dose regimens [e.g., AVO (5 mg/kg) and 100 Gy] result in modest tumor shrinkage, with a higher proportion of patients classified as SD. As AVO doses increase [e.g., AVO (40 mg/kg) and 50 Gy], tumor shrinkage becomes more pronounced, reflected by a larger fraction of patients achieving PR and a marked reduction in SD cases. This highlights the potential of AVO to reduce the reliance on high radiation doses while maintaining or even improving treatment outcomes. Notably, the combination regimens show a clear advantage over RT monotherapy, which achieves only modest tumor control. Incorporation of AVO not only improves PR rates but also reduces the proportion of patients with SD or PD, shifting the outcome distribution more favorably toward tumor shrinkage across the virtual patient cohort.

DISCUSSION

Over the past two decades, multiple therapeutic approaches, such as surgery, chemotherapy, and radiation, have been used to enhance treatment outcomes and survival rates in pediatric patients with MRT and Atypical Teratoid/Rhabdoid Tumor (ATRT). RT remains the mainstay of treatment for both cranial and extracranial rhabdoid tumors. However, despite major efforts, significant advances remain elusive, especially in patients less than 3 years old due to long-term toxicities from the high doses of RT and chemotherapy required to achieve meaningful responses (*4*, *47*). Thus, there has been an increasing interest in exploring therapeutic strategies to maximize RT efficiency at lower doses to minimize immediate and long-term radiotoxicity in pediatric MRT management. However, new drug discovery is scientifically and financially challenging for rare tumors like MRT and ATRT. Thus, drug repurposing is an attractive strategy. AVO is an FDA-approved antimalarial drug and has been reported for the treatment of various adult malignancies including breast cancer (*23*), renal cell carcinoma (*48*), non–small cell lung cancer (*22*), aggressive thyroid cancer (*49*), and leukemia (*50*), both as monotherapy and in combination with chemoradiation. However, to the best of our knowledge, this is one of the earliest studies using AVO to enhance radiosensitivity in pediatric cancer treatment and management.

Our findings in this study unequivocally demonstrate the benefit of combining AVO with RT to achieve complete, durable therapeutic responses in MRT xenografts, at low, clinically viable doses. Our

results revealed that short-term (7-day) AVO treatment at pharmacologically viable doses could effectively improve the oxygenation levels in A-204 tumors (Fig. 3) and thereby result in long-term inhibition of tumor growth when combined with a single 10-Gy x-ray dose (Fig. 5). This phenomenon was confirmed by our histopathological data. Additionally, compared to the saline-treated group, the lower Ki-67 signal (Fig. 4) and higher γ-H2AX signal (Fig. 6) further validated that the combination therapy enhanced DNA damage and cell apoptosis, ultimately inhibiting tumor growth. Most notably, for the AVO and RT treatment groups, all the tumors were completely abolished within 10 days posttreatment and did not recur for the remainder of the study. Our approach demonstrated exceptional treatment outcomes when compared to other MRT treatment methods, as most existing strategies can only inhibit tumor growth without fully eliminating them (*51*, *52*), showing that a negligible pimonidazole signal was observed in the AVO-treated groups (Fig. 4).

There are several advantages to our treatment strategy: (i) Although multiple treatment strategies including immunotherapy and targeted therapy have been explored in recent years to improve the survival rates of patients with MRT, conducting comprehensive studies of these treatment strategies remains challenging due to the rarity of pediatric MRT and limited patient samples. Thus, the traditional combination of chemotherapy and RT for treating patients with MRT would be the quickest approach to investigate further and implement in clinical practice. (ii) Before a new drug can be administered to clinical patients with MRT, several critical steps must be completed, including preclinical studies, an Investigational New Drug application, clinical trials (phases 1 to 3), a New Drug Application, regulatory approval, and post-market surveillance (*53*). Given that most patients with rhabdoid tumors are under 3 years old, using an orally bioavailable, FDA-approved, off-label drug, AVO to radiosensitize MRT in the clinic can be easily and quickly envisaged, as opposed to other radiosensitizers now under development that would need to undergo a long-term approval. Additionally, our data demonstrate that AVO exhibits effects at significantly lower concentrations (EC_{50} = 28.36 μM; Fig. 2A) than that of metformin (EC_{50} = 13.15 Mm; fig. S5) and another complex I inhibitor, phenformin (*54*). Therefore, although safe for use, these biguanides have resulted in suboptimal efficacy in clinical trials. Another preclinical inhibitor of mitochondrial respiratory complex I, IACS-010759, has been associated with multiple side effects such as neurological symptoms (*55*), hematologic toxicity, metabolic disturbances, weight loss, and nausea and vomiting (*56*), owing to extremely narrow therapeutic indices. Both phenformin and IACS-010759 were withdrawn from clinical trials due to a heightened risk of fatal lactic acidosis (*54*, *55*), resulting from a shift toward glycolysis that induces increased lactic acid production. Our preliminary metabolic analysis does not indicate an obvious glycolytic shift in A-204 cells even after prolonged AVO exposure (Fig. 8 and fig. S2), which bodes well for its translation to pediatric patients. Moreover, our data monitoring mouse body weight (Fig. 5B) and histopathology of off-target organs (Fig. 6D) demonstrate that AVO does not cause noticeable systemic toxicity. Additionally, as an off-label drug, cost-effectiveness of AVO can double the impact to patients suffering from this disease, especially considering the small patient cohorts. Therefore, considering all the benefits, AVO stands out as the optimal mitochondrial inhibitor in pediatric MRT management (*3*). Local RT was used in this work. This targeted and precise treatment allows for highly accurate radiation delivery, reducing side effects and enhancing treatment outcomes by focusing directly on the tumor while minimizing damage to surrounding health tissues. Our data establish that AVO can integrate both with single dose and fractionated RT regimens with ease and without changes to its effectiveness. Most excitingly, AVO reduces the effective local radiation dose required to achieve maximum and durable therapeutic effect, which makes RT safer for pediatric patients both in the long and short terms.

Another core feature of our work is the adoption of noninvasive MSOT imaging to map the spatiotemporal changes in pediatric rhabdoid tumors, in response to AVO. Our imaging results suggest that the real-time changes in oxygenation could be visualized and monitored before, during, and after the treatment with high fidelity and reproducibility. MSOT is a safe, widely available, and ionizing radiation-free imaging modality, which can inform tumor oxygenation status in a label-free manner. By performing $\%sO_2$ measurements following a switch of 21% oxygen to 100% oxygen, ΔsO_2 was measured using the oxygen-enhanced (OE-MSOT) procedure. Our data indicate the potential of ΔsO_2 to serve as both a pharmacodynamic biomarker measuring the magnitude and duration of hypoxia resolution by AVO and a biomarker to indicate the onset of resistance to the drug. We show that, although potent, hypoxia alleviation by AVO is transient, which necessitates careful timing of RT. As it is free from ionizing radiation, we posit that MSOT can be easily and safely implemented to guide and optimize treatment schedules, as well as evaluate treatment response of AVO-enhanced RT in pediatric patients with MRT, enabling real-time, personalized treatment adjustments. These studies fill an unmet gap in the design and implementation of smart, data-driven combination therapies, particularly for children and young adults where poorly designed treatments can lead to devastating acute and chronic toxicities. OE-MSOT has the potential in refining the administration of anticancer therapies, especially by optimizing the timing of sequential treatments and distinguishing between responsive and unresponsive tumors. Furthermore, frequent monitoring enabled by an ionizing radiation-free imaging modality would spare the pediatric patients from ineffective or toxic overtreatment. Although clinical trials with AVO are now underway in adult cancers (*22*), the results of our study provide a strong foundation for advancing the drug to benefit children with rhabdoid tumors and other radioresistant cancers.

Last, to extrapolate our preclinical findings to human patients, we have developed mathematical models to predict human responses as well as determine optimal AVO and RT dosing and timing combinations. By bridging preclinical and clinical settings, these first-in-patient simulations underscore the model's utility for predicting patient-specific outcomes and optimizing treatment strategies. The inclusion of inter-patient variability in the virtual cohort ensures robustness of the predictions, supporting future clinical trial designs that aim to refine dosing regimens and schedules based on expected clinical response rates. By integrating both tumor response trajectories and categorical outcome distributions, our data (Fig. 10F) provide a comprehensive view of how optimized regimens can shift the balance toward more favorable outcomes in a virtual patient cohort. These findings reinforce the importance of tailoring dosing strategies to maximize treatment efficacy while minimizing the potential for radiation-induced toxicity.

Our mathematical model has some limitations that warrant consideration. First, the inability of the model to achieve complete response (CR) is rooted in its mathematical structure. By design, the model describes tumor dynamics using continuous differential equations, where tumor volume can asymptote toward zero but never

reach it exactly. As a result, any residual tumor volume, however small, persists at the end of the simulation and can regrow over time, preventing complete regression. To address this, one could redefine CR on the basis of a practical threshold, such as a 99% reduction in tumor volume. However, for simplicity, we chose to focus on PR, which is a clinically relevant metric aligned with Response Evaluation Criteria in Solid Tumors (RECIST) 1.1 guidelines. The translational relevance of the findings would also benefit from further validation using clinical datasets. The optimization studies explored fixed dose schedules, but adaptive treatment strategies and considerations of healthy tissue toxicity remain areas for future exploration. Last, we recognize that children and infants are not small adults, and the differences are not merely body weight dependent but rooted in physiological and biochemical differences (*57*). Thus, for simplicity, our virtual patient cohort is generated by taking an adult human patient into account (70 kg), which may not fully capture the complexities of translating the combination therapy in the pediatric setting. Addressing these limitations in future studies will enhance the model's applicability and translational value.

MATERIALS AND METHODS

Data acquisition and processing of mRNA sequencing expression profiles

We downloaded the transcriptomic data from National Cancer Institute Therapeutically Applicable Research to Generate Effective Treatments - Rhabdoid Tumor project (https://portal.gdc.cancer.gov/projects/TARGET-RT) within the GDC Data Portal (Data Release 37.0, 29 March 2023) using The Cancer Genome Atlas biolinks R package (https://bioconductor.org/packages/release/bioc/html/TCGAbiolinks.html). Raw counts and sample metadata were loaded in the R environment using the Huntsman Cancer Institute (hciR) package (https://github.com/HuntsmanCancerInstitute/hciR) of the University of Utah. Sixty-three patients with rhabdoid cancer, all aged between 0 and 14 years, were selected. Log_2 normalization was performed for further analysis. ssGSEA was performed on the basis of Hallmark gene sets. Enrichment scores for all pathways are plotted in a heatmap, categorized by the different stages of patients with rhabdoid tumor.

To plot survival curves, we first loaded the R package – survival: survival analysis (version 3.7-0) and ran the Cox proportional hazards regression modeling on all samples. We then looped through all 230 OXPHOS genes [OXPHOS gene signature; Kyoto Encyclopedia of Genes and Genomes (KEGG) database], applying the Cox proportional hazards model to obtain the Cox coefficients and *P* values. Next, we ranked the OXPHOS genes and identified those with significant *P* values ($P < 0.05$), indicating a difference in survival rates based on high or low gene expression. Last, we plotted survival curves for these genes by dividing the survival data into high- and low-expression groups on the basis of the median and included the *P* value in the plot.

Cell lines and compounds

Human rhabdoid tumor A-204 cell line (HTB-82) was purchased from the American Type Culture Collection (ATCC). Cells were cultured at 37°C with 5% CO_2 in McCoy's 5A medium (ATCC) supplemented with 10% fetal bovine serum (GenClone) and 1% penicillin-streptomycin (GenClone). AVO was obtained from Thermo Fisher Scientific. Bovine serum albumin (BSA) was obtained from Sigma-Aldrich. Matrigel was obtained from Huntsman Cancer Institute Preclinical Research Resource. Pimonidazole hydrochloride and Red 549 monoclonal antibody (mAb) were obtained from Hypoxyprobe. Purified rat anti-mouse CD31 (catalog no. 550274) was purchased from BD Biosciences. Alexa Fluor 488 AffiniPure Donkey Anti-Rat IgG (H+L) (Lot 163136) and Rhodamine [tetramethyl rhodamine isothiocyanate (TRITC)] AffiniPure Donkey Anti-Rat IgG (H+L) (Lot 157518) were obtained from Jackson ImmunoResearch Inc. Histone H2AX antibody (NB100-384) was purchased from Novus Biologicals and secondary antibody Donkey Anti-Rabbit IgG (H+L) Dylight594 (SA5-10040) from Invitrogen. Purified anti-mouse/human Ki-67 antibody (151202) was purchased from BioLegend. The 2,5-diphenyltetrazolium bromide (MTT) assay (M6494) was obtained from Thermo Fisher Scientific. To model acquired resistance, AVO-resistant A-204 cell line (A^R-A-204) was established in house by gradient AVO treatment following slight modifications of previously published protocols (*58*).

Cell viability assay

To determine the cytotoxicity of AVO, MTT assay was carried out in A-204 and A^R-A-204 cells. The cells were seeded at a density of 2000 cells per well in a 96-well plate and cultured in McCoy's 5A culture medium at 37°C with 5% CO_2. After 24 hours of incubation, cells in each well were treated with various concentrations of AVO (5, 10, 20, 50, 100, 200, and 500 μM) in 100 μl of culture medium, with each concentration tested in six replicates. Following 72 hours of AVO treatment, MTT solution (10% 12 mM MTT stock solution) was added to each well and incubated for 4 hours. The medium was then removed, and 50 μl of DMSO was added to each well. The cells were incubated for an additional 10 min at 37°C. The absorbance at 540 nm was determined using a microplate reader (Cytation 3, BioTek, USA), and the cell viability was calculated using the following equation

$$\text{Cell viability (\%)} = \left[\frac{A_s - A_b}{A_c - A_b}\right] \times 100$$

where A_s is absorbance of test well, A_b is absorbance of blank (medium only), and A_c is absorbance of control (cells only).

Seahorse experiment

Real-time OCRs and ECARs for A-204 and A^R-A-204 cells treated with AVO were determined using the XFPro Analyzer (Seahorse Biosciences). A-204 and A^R-A-204 cells were seeded in the Seahorse XF Pro cell culture microplate at a density of 20,000 cells per well and cultured at 37°C with 5% CO_2 in McCoy's 5A medium for 24 hours to allow attachment. Then, both A-204 and A^R-A-204 cells were treated with 25 μM AVO for 24 hours. Control groups treated with DMSO alone were processed in parallel. The measurements of the OCR were taken in XF assay medium containing 10 mM glucose. Pyruvate (1 mM) and L-glutamine (2 mM) and oligomycin (1 μM), FCCP (0.5 μM), and rotenone/antimycin A (0.5 μM) were added sequentially for OCR measurement. ECAR measurements were taken in XF assay medium containing 1 mM pyruvate and 2 mM L-glutamine. Glucose (10 mM), oligomycin (2 μM), and 2-DG (100 mM) were added for ECAR into the injection ports in the XF Pro sensor cartridge. AVO (25 μM) was added into each well (excluding the DMSO wells) for the duration of the seahorse experiment. Measurements were normalized cell numbers, counted by adding 2 μM Hoechst 33342.

Animal models and treatments

Six- to 8-week-old female athymic nude mice [Crl:NU(NCr)-*Foxn1*^{nu}] were purchased from Charles River Laboratories. All animal experiments were conducted in accordance with the approved protocol by the Institutional Animal Care and Use Committee at the University of Utah (protocol number 21-11013). Wild-type A-204 (1×10^6) cells or AVO-resistant A^R-A-204 (1×10^6) cells [in phosphate-buffered saline (PBS):Matrigel = 1:1 solution] were inoculated subcutaneously in 26- to 44-day-old athymic nude female mice. When the tumors reached around 50 mm^3, mice were randomized into treatment groups ($n = 5$) that were given saline (control), AVO, RT (10 Gy), or the combination treatment of AVO followed by RT. AVO was administered as an oral suspension of 50 mg kg^{-1} dose per day via oral gavage, following clinical dosing schedule (*59*). Mice were given this dose for 7 days because AVO typically requires 1 or 2 weeks to achieve a consistent plasma concentration in human patients (*60*, *61*). Mice in RT or combination treatment cohorts received a single dose of 10-Gy x-ray irradiation focused on the tumor (Rad Source Technologies, USA) after 7 days of AVO treatment. A separate cohort of mice was also treated with 30-Gy dose either alone (in fractions of 6 Gy over 5 days) or in combination with AVO.

Mice were monitored for welfare throughout the study, and body weights were collected every day. Tumor size was measured with calipers, and volume was calculated with the formula: $[V = (W^2 \times L)/2]$. Mice were euthanized (study endpoint) once the tumor reached 1000 mm^3 or if the body weight dropped 20% relative to baseline or if the mice were under poor bodily condition. After sacrifice, tumors and other organs were excised 1 hour after intraperitoneal administration of pimonidazole hydrochloride (60 mg kg^{-1}). A^R-A-204 tumor-bearing mice were subjected to the same procedures.

In vivo MSOT

All in vivo MSOT experiments were performed using iThera inVision 256-TF MSOT System (iThera Medical GmBH). MSOT scans were performed 1 day prior treatment (referred to as day −1 when the tumors reached to ~50 mm^3) for all groups to establish baseline. Subsequently, for the saline- and AVO-treated groups, longitudinal MSOT was conducted on days 3, 9, and 23 posttreatment. For the 10 Gy– and AVO and 10 Gy–treated groups, MSOT scans were conducted on days 3, 9, 16, and 30.

Briefly, A-204 or A^R-A-204 tumor-bearing mice were anesthetized using isoflurane, and tail veins were catheterized. A thin layer of ultrasound gel (Aquasonic Clear, Parker Labs) was applied to facilitate optical and acoustic coupling with the polyethylene membrane. Subsequently, the mice were positioned in a lateral, side-lying orientation in a bag for imaging purposes. The chamber temperature was adjusted to 36°C, and the mice were allowed to equilibrate to the temperature for 10 min before imaging. This temperature allowed the mice to maintain 37°C body temperature for the duration of the scan. Images were acquired at the largest tumor cross section of the mice with a step size of 1 mm. OE-DCE MSOT imaging was performed in the same scan session, following our previously published protocols (*30*). For OE-MSOT scan, images were first acquired at 700-, 730-, 760-, 800-, 850-, and 875-nm wavelengths with 21% O_2 (air) breathing gas for 2 min. Ten frames and 20 repetitions were recorded at every imaging wavelength. The breathing gas was switched to 100% O_2. To allow the mice to reach equilibrium, the mice remained in the chamber for 2 min without imaging. A second set of images was collected with 100% O_2 breathing gas for 2 min using the same parameters.

For DCE-MSOT scans, images were acquired at 700-, 730-, 760-, 800-, 850-, and 875-nm wavelengths under 100% O_2 breathing gas. Ten frames and 141 repetitions were recorded at every imaging wavelength. After 1 min of acquiring preinjection baseline images, ICG (Sigma-Aldrich, 300 nmol, 100 μl) was intravenously injected, and mice were scanned continuously for an additional 15 min. ViewMSOT (version 4.0) was used for image processing. Images were reconstructed using the model linear algorithm and fluence corrected (only for OE-MSOT scans) according to vendor presets. Spectral unmixing extracted the relative contribution of oxyhemoglobin (HbO_2) and deoxyhemoglobin (Hb), which were then used to produce blood oxygen saturation measurements ($\%sO_2^{air}$ and $\%sO_2^{O2}$) with each breathing gas. The difference between the average $\%sO_2^{air}$ and $\%sO_2^{O2}$ during their respective 2-min acquisitions was then used to determine ΔsO_2 within the tumor. For the DCE-MSOT scan, the pharmacokinetic rates of uptake (NK^{trans}) and washout (K_{ep}) of ICG were computed using our fluence-independent image analysis protocol (*30*, *62*). All parametric analyses for OE-DCE-MSOT scans were performed in MATLAB R2021b using our custom code (available upon request).

Histological analysis

Tissues prepared for immunofluorescence were rinsed in PBS and preserved in optimal cutting temperature (OCT; Fisher HealthCare, USA) at −80°C. Tissues were cryo-sectioned into 5-μm-thick sections (ARUP Laboratories, University of Utah) and stored at −80°C for further use. Before use, tissue sections were fixed with cold 4% paraformaldehyde (PFA) for 10 min and washed twice in PBS, followed by incubation in blocking buffer (5% BSA in PBS supplemented with 0.1% Tween 20) for 1 hour. For pimonidazole staining, sections were stained with Red 549 dye mAb (1:100, diluted in blocking buffer) overnight at 4°C and thoroughly washed twice in PBS. For CD31, γ-H2AX, and Ki-67 staining, tissues were first incubated overnight at 4°C with primary rat anti-mouse CD31 (1:100, diluted in blocking buffer), primary rabbit γ-H2AX (1:100, diluted in blocking buffer), or primary rat anti-mouse/human Ki-67 (1:100, diluted in blocking buffer), respectively. After washing twice with PBS, the sections were incubated for 1 hour at room temperature with secondary antibodies: Alexa Fluor 488 Affinipure Donkey Anti-Rat IgG (H+L) (1:200, diluted in blocking buffer), Dylight594 Donkey Anti-Rabbit IgG (H+L) (1:200, diluted in blocking buffer), or TRITC Affinipure Donkey Anti-Rat IgG (H+L) (1:200, diluted in blocking buffer) for CD31, γ-H2AX, and Ki-67, respectively. Sections were washed twice in PBS, stained with 4′,6-diamidino-2-phenylindole (1 μg/ml) for 10 min, followed by mounting buffer. All slides were stored at 4°C in a light-protected environment. Fluorescence images were acquired with the confocal laser scanning microscope (CLSM, Leica, SP8). At least five separate regions were imaged per tissue, and three mice per group were analyzed for histological experiments. Whole-tissue images were obtained on an Axioscan 7 slide scanner. For histological evaluation of tissues, 5-μm sections were obtained from the OCT cassettes and subsequently used for H&E staining. Slides were scanned at 40× resolution using the Olympus biological microscope (Olympus BX41), and the images were processed using AmScope software.

Mathematical model development

We developed a mathematical framework to elucidate the dynamic interplay between tumor growth, radiotherapy, and pharmacological intervention with AVO in MRT. Expanding upon our prior mechanistic model (*63*–*65*), the current model integrates tumor growth dynamics, drug pharmacokinetics, and the modulation of $\%sO_2$ within hypoxic tumor microenvironments, thereby capturing the biological processes that influence treatment efficacy.

TSE curve

The TSE curve relates the radiation dose ($Dose_{rad}$) to the AVO dose ($Dose_{AVO}$) required to maintain tumor stasis, defined by $dV(t)/dt = 0$ (*44*–*46*). At $dV(t)/dt = 0$, tumor growth is exactly countered by treatment effects, resulting in a stable tumor size. By examining this curve, we can quantify how increases in AVO dose reduce the radiation dose needed to achieve tumor stasis, thereby providing insights into the synergistic interaction between AVO-mediated oxygenation enhancement and RT.

Assuming a single dose of AVO and a steady-state approximation for its pharmacokinetics, the relationship between $Dose_{rad}$ and $Dose_{AVO}$ is derived as

$$\mathrm{Dose}_{\mathrm{rad}} = \frac{\gamma}{\delta_{\max}-\gamma}\cdot D_{50}^{\mathrm{theoretical}}\cdot\left(\frac{\mathrm{SpO}_2^{\mathrm{basal}}+\left(100-\mathrm{SpO}_2^{\mathrm{basal}}\right)\cdot e^{-\alpha\cdot\frac{\mathrm{Dose}_{\mathrm{AVO}}\cdot F}{V_d}}}{\mathrm{SpO}_2^{\mathrm{basal}}}\right)^{\beta} \quad (1)$$

Full derivation details are provided in the Supplementary Materials.

To generate the TSE curve, we solved Eq. 1 for 500 values of $Dose_{AVO}$ ranging from 0 to 10 mg/kg, calculating the corresponding $Dose_{rad}$ values for each point. We then repeated this process 50 times, each time randomly sampling parameters from the mouse-based parameter distributions obtained during model calibration. Parameters were sampled using Latin hypercube sampling to capture inter-animal variability. The mean value and 95% confidence intervals of all simulations were obtained and plotted to illustrate the relationship between $Dose_{AVO}$ and $Dose_{rad}$. This approach incorporates interindividual variability and provides a rigorous means to evaluate how varying AVO dosing can reduce the required radiation dose, offering quantitative insights into potential synergistic treatment strategies.

Interspecies scaling

To evaluate the translational potential of our framework for predicting AVO pharmacokinetics and tumor response dynamics, we extrapolated the mouse model to humans. This was achieved by substituting mouse-specific parameter values with human population averages from the literature (*66*) or by applying allometric scaling to parameters derived from the mouse model. The scaling was performed as

$$P_i^{\mathrm{h}} = P_i^{\mathrm{m}}\cdot\left(\frac{\mathrm{BW_h}}{\mathrm{BW_m}}\right)^{\theta} \quad (2)$$

where, P_i^{h} and P_i^{m} is the value of parameter i for humans and mice, respectively; and $\mathrm{BW_h}$ and $\mathrm{BW_m}$ is the body weight of humans (70 kg) and mice (0.02 kg), respectively. The allometric scaling exponent (θ) varies depending on the parameter type. For rate constants such as the tumor growth rate (γ) and maximum radiation-induced cell death rate (δ_{max}), θ was set to −0.25. For parameters related to the drug, including the sensitivity of oxygenation to AVO (α) and clearance (Cl), θ was set to 0.75. For the volume of distribution (V_d), θ was set to 1. This approach ensures a physiologically consistent extrapolation of pharmacokinetic and dynamic parameters from mice to humans, enabling a preliminary assessment of how AVO dosing and tumor responses might translate to clinical contexts.

Tumor response evaluation metrics

Tumor response to treatment was evaluated on the basis of percentage changes in tumor diameter relative to baseline, consistent with clinical standards such as the RECIST 1.1 criteria (*67*). In our simulations, the tumor was assumed to be spherical, and the diameter [$d(t)$] was defined as the diameter of the sphere at a given time point. The percentage change in tumor diameter (Δd) was calculated as

$$\Delta d = \frac{d_{\mathrm{final}} - d_{\mathrm{baseline}}}{d_{\mathrm{baseline}}}\cdot 100$$

where d_{baseline} is tumor diameter at the start of treatment and d_{final} is the diameter at the end of the simulation period (i.e., 30 days after treatment completion). Tumor responses were categorized as follows: CR was defined as the disappearance of the tumor; PR was defined as $\Delta d \leq -30\%$, representing a reduction of 30% or more in tumor diameter relative to baseline; SD was defined as a change of $-30\% < \Delta d < +20\%$; and PD was defined as $\Delta d \geq +20\%$, corresponding to an increase of 20% or more in tumor diameter relative to baseline.

This metric provides a clinically relevant evaluation of treatment efficacy by focusing on changes in tumor dimensions rather than volumes. By aligning with clinical standards for tumor response, this method enhances the translational potential of the results.

Optimization of treatment protocols

To identify optimal treatment strategies, we conducted two sets of optimization experiments: (i) determining the best timing for initiating RT relative to AVO administration and (ii) identifying clinically optimal dose combinations of AVO and radiation that minimize total radiation exposure while achieving effective tumor control. Both sets of experiments used the virtual patient cohort of 500 individuals, and tumor response was evaluated on the basis of percentage change in tumor diameter (Δd) 1 month after the end of treatment, consistent with RECIST 1.1 criteria. The fraction of patients achieving a PR ($\Delta d \leq -30\%$) was used as the primary outcome metric. Additionally, to assess the impact of AVO administration frequency on treatment outcomes, simulations included two AVO dosing schedules: daily and once every 2 days. The details can be found in the Supplementary Materials.

Statistics

All data represent at least three biological replicates. Statistical analysis was conducted using GraphPad Prism 8 software (GraphPad Software Inc.). The data were analyzed using unpaired t tests and one-way analysis of variance (ANOVA; multiple comparisons). Statistical significance between two groups was determined with two-tailed P values: $^{*}P < 0.05$, $^{**}P < 0.01$, $^{***}P < 0.001$, and $^{****}P < 0.0001$. Survival was estimated by comparison of Kaplan-Meier curves using a log-rank test.

Supplementary Materials

This PDF file includes:

Supplementary Methods
Figs. S1 to S15
Table S1
References

REFERENCES AND NOTES

1. D. L. Buscariollo, H. S. Park, K. B. Roberts, J. B. Yu, Survival outcomes in atypical teratoid rhabdoid tumor for patients undergoing radiotherapy in a Surveillance, Epidemiology, and End Results analysis. *Cancer* **118**, 4212–4219 (2012).
2. A. Biswas, L. Kashyap, A. Kakkar, C. Sarkar, P. K. Julka, Atypical teratoid/rhabdoid tumors: Challenges and search for solutions. *Cancer. Manag. Res.* **8**, 115–125 (2016).
3. S. K. Wang, P. Mannam, K. Dukleska, F. Balarezo, Congenital disseminated malignant rhabdoid tumor mimicking a vascular lesion. *Cureus* **16**, e58337 (2024).
4. K. Nemes, P. D. Johann, S. Tüchert, P. Melchior, C. Vokuhl, R. Siebert, R. Furtwängler, M. C. Frühwald, Current and emerging therapeutic approaches for extracranial malignant rhabdoid tumors. *Cancer. Manag. Res.* **14**, 479–498 (2022).
5. R. G. Majzner, J. L. Theruvath, A. Nellan, S. Heitzeneder, Y. Cui, C. W. Mount, S. P. Rietberg, M. H. Linde, P. Xu, C. Rota, E. Sotillo, L. Labanieh, D. W. Lee, R. J. Orentas, D. S. Dimitrov, Z. Zhu, B. S. Croix, A. Delaidelli, A. Sekunova, E. Bonvini, S. S. Mitra, M. M. Quezado, R. Majeti, M. Monje, P. H. B. Sorensen, J. M. Maris, C. L. Mackall, CAR T cells targeting B7-H3, a pan-cancer antigen, demonstrate potent preclinical activity against pediatric solid tumors and brain tumors. *Clin. Cancer Res.* **25**, 2560–2574 (2019).
6. J. Theruvath, E. Sotillo, C. W. Mount, C. M. Graef, A. Delaidelli, S. Heitzeneder, L. Labanieh, S. Dhingra, A. Leruste, R. G. Majzner, P. Xu, S. Mueller, D. W. Yecies, M. A. Finetti, D. Williamson, P. D. Johann, M. Kool, S. Pfister, M. Hasselblatt, M. C. Frühwald, O. Delattre, D. Surdez, F. Bourdeaut, S. Puget, S. Zaidi, S. S. Mitra, S. Cheshier, P. H. Sorensen, M. Monje, C. L. Mackall, Locoregionally administered B7-H3-targeted CAR T cells for treatment of atypical teratoid/rhabdoid tumors. *Nat. Med.* **26**, 712–719 (2020).
7. J. Torchia, B. Golbourn, S. Feng, K. C. Ho, P. Sin-Chan, A. Vasiljevic, J. D. Norman, P. Guilhamon, L. Garzia, N. R. Agamez, M. Lu, T. S. Chan, D. Picard, P. de Antonellis, D. A. Khuong-Quang, A. C. Planello, C. Zeller, D. Barsyte-Lovejoy, L. Lafay-Cousin, L. Letourneau, M. Bourgey, M. Yu, D. M. A. Gendoo, M. Dzamba, M. Barszczyk, T. Medina, A. N. Riemenschneider, A. S. Morrissy, Y. S. Ra, V. Ramaswamy, M. Remke, C. P. Dunham, S. Yip, H. K. Ng, J. Q. Lu, V. Mehta, S. Albrecht, J. Pimentel, J. A. Chan, G. R. Somers, C. C. Faria, L. Roque, M. Fouladi, L. M. Hoffman, A. S. Moore, Y. Wang, S. A. Choi, J. R. Hansford, D. Catchpoole, D. K. Birks, N. K. Foreman, D. Strother, A. Klekner, L. Bognár, M. Garami, P. Hauser, T. Hortobágyi, B. Wilson, J. Hukin, A. S. Carret, T. E. Van Meter, E. I. Hwang, A. Gajjar, S. H. Chiou, H. Nakamura, H. Toledano, I. Fried, D. Fults, T. Wataya, C. Fryer, D. D. Eisenstat, K. Scheinemann, A. J. Fleming, D. L. Johnston, J. Michaud, S. Zelcer, R. Hammond, S. Afzal, D. A. Ramsay, N. Sirachainan, S. Hongeng, N. Larbcharoensub, R. G. Grundy, R. R. Lulla, J. R. Fangusaro, H. Druker, U. Bartels, R. Grant, D. Malkin, C. J. McGlade, T. Nicolaides, T. Tihan, J. Phillips, J. Majewski, A. Montpetit, G. Bourque, G. D. Bader, A. T. Reddy, G. Y. Gillespie, M. Warmuth-Metz, S. Rutkowski, U. Tabori, M. Lupien, M. Brudno, U. Schüller, T. Pietsch, A. R. Judkins, C. E. Hawkins, E. Bouffet, S. K. Kim, P. B. Dirks, M. D. Taylor, A. Erdreich-Epstein, C. H. Arrowsmith, D. D. De Carvalho, J. T. Rutka, N. Jabado, A. Huang, Integrated (epi)-genomic analyses identify subgroup-specific therapeutic targets in CNS rhabdoid tumors. *Cancer Cell* **30**, 891–908 (2016).
8. J. M. Maris, C. L. Morton, R. Gorlick, E. A. Kolb, R. Lock, H. Carol, S. T. Keir, C. P. Reynolds, M. H. Kang, J. Wu, M. A. Smith, P. J. Houghton, Initial testing of the aurora kinase A inhibitor MLN8237 by the Pediatric Preclinical Testing Program (PPTP). *Pediatr. Blood Cancer* **55**, 26–34 (2010).
9. M. F. Weingart, J. J. Roth, M. Hutt-Cabezas, T. M. Busse, H. Kaur, A. Price, R. Maynard, J. Rubens, I. Taylor, X. G. Mao, J. Xu, Y. Kuwahara, S. J. Allen, A. Erdreich-Epstein, B. E. Weissman, B. A. Orr, C. G. Eberhart, J. A. Biegel, E. H. Raabe, Disrupting LIN28 in atypical teratoid rhabdoid tumors reveals the importance of the mitogen activated protein kinase pathway as a therapeutic target. *Oncotarget* **6**, 3165–3177 (2015).
10. A. D. Trobaugh-Lotrario, M. J. Finegold, J. H. Feusner, Rhabdoid tumors of the liver: Rare, aggressive, and poorly responsive to standard cytotoxic chemotherapy. *Pediatr. Blood Cancer* **57**, 423–428 (2011).
11. D. A. Rodeberg, M. D. Wharam, E. R. Lyden, J. A. Stoner, K. Brown, S. L. Wolden, C. N. Paidas, S. S. Donaldson, D. S. Hawkins, S. L. Spunt, C. A. Arndt, Delayed primary excision with subsequent modification of radiotherapy dose for intermediate-risk rhabdomyosarcoma: A report from the Children's Oncology Group Soft Tissue Sarcoma Committee. *Int. J. Cancer* **137**, 204–211 (2015).
12. V. Jairam, K. B. Roberts, J. B. Yu, Historical trends in the use of radiation therapy for pediatric cancers: 1973-2008. *Int. J. Radiat. Oncol. Biol. Phys.* **85**, e151–e155 (2013).
13. A. Rakotomalala, A. Escande, A. Furlan, S. Meignan, E. Lartigau, Hypoxia in solid tumors: How low oxygenation impacts the "Six Rs" of radiotherapy. *Front. Endocrinol.* **12**, 742215 (2021).
14. H. Scholz, F. J. Boivin, K. M. Schmidt-Ott, S. Bachmann, K.-U. Eckardt, U. I. Scholl, P. B. Persson, Kidney physiology and susceptibility to acute kidney injury: Implications for renoprotection. *Nat. Rev. Nephrol.* **17**, 335–349 (2021).
15. C. M. Neophytou, M. Panagi, T. Stylianopoulos, P. Papageorgis, The role of tumor microenvironment in cancer metastasis: Molecular mechanisms and therapeutic opportunities. *Cancers* **13**, 2053 (2021).
16. A. Sebestyén, L. Kopper, T. Dankó, J. Tímár, Hypoxia signaling in cancer: From basics to clinical practice. *Pathol. Oncol. Res.* **27**, 1609802 (2021).
17. W. Bouleftour, E. Rowinski, S. Louati, S. Sotton, A. S. Wozny, P. Moreno-Acosta, B. Mery, C. Rodriguez-Lafrasse, N. Magne, A review of the role of hypoxia in radioresistance in cancer therapy. *Med. Sci. Monit.* **27**, e934116 (2021).
18. C. Peitzsch, R. Perrin, R. P. Hill, A. Dubrovska, I. Kurth, Hypoxia as a biomarker for radioresistant cancer stem cells. *Int. J. Radiat. Biol.* **90**, 636–652 (2014).
19. P. Marchetti, Q. Fovez, N. Germain, R. Khamari, J. Kluza, Mitochondrial spare respiratory capacity: Mechanisms, regulation, and significance in non-transformed and cancer cells. *FASEB J.* **34**, 13106–13124 (2020).
20. R. H. Farnsworth, M. Lackmann, M. G. Achen, S. A. Stacker, Vascular remodeling in cancer. *Oncogene* **33**, 3496–3505 (2014).
21. K. Matuszewska, M. Pereira, D. Petrik, J. Lawler, J. Petrik, Normalizing tumor vasculature to reduce hypoxia, enhance perfusion, and optimize therapy uptake. *Cancers* **13**, 4444 (2021).
22. M. Skwarski, D. R. McGowan, E. Belcher, F. Di Chiara, D. Stavroulias, M. McCole, J. L. Derham, K. Y. Chu, E. Teoh, J. Chauhan, D. O'Reilly, B. H. L. Harris, P. S. Macklin, J. A. Bull, M. Green, G. Rodriguez-Berriguete, R. Prevo, L. K. Folkes, L. Campo, P. Ferencz, P. L. Croal, H. Flight, C. Qi, J. Holmes, J. P. B. O'Connor, F. V. Gleeson, W. G. McKenna, A. L. Harris, D. Bulte, F. M. Buffa, R. E. Macpherson, G. S. Higgins, Mitochondrial inhibitor atovaquone increases tumor oxygenation and inhibits hypoxic gene expression in patients with non-small cell lung cancer. *Clin. Cancer Res.* **27**, 2459–2469 (2021).
23. M. Fiorillo, R. Lamb, H. B. Tanowitz, L. Mutti, M. Krstic-Demonacos, A. R. Cappello, U. E. Martinez-Outschoorn, F. Sotgia, M. P. Lisanti, Repurposing atovaquone: Targeting mitochondrial complex III and OXPHOS to eradicate cancer stem cells. *Oncotarget* **7**, 34084–34099 (2016).
24. T. M. Ashton, E. Fokas, L. A. Kunz-Schughart, L. K. Folkes, S. Anbalagan, M. Huether, C. J. Kelly, G. Pirovano, F. M. Buffa, E. M. Hammond, M. Stratford, R. J. Muschel, G. S. Higgins, W. G. McKenna, The anti-malarial atovaquone increases radiosensitivity by alleviating tumour hypoxia. *Nat. Commun.* **7**, 12308 (2016).
25. S. Dey, S. Kumari, S. P. Kalainayakan, J. Campbell III, P. Ghosh, H. Zhou, K. E. FitzGerald, M. Li, R. P. Mason, L. Zhang, L. Liu, The vascular disrupting agent combretastatin A-4 phosphate causes prolonged elevation of proteins involved in heme flux and function in resistant tumor cells. *Oncotarget* **9**, 4090–4101 (2018).
26. L. J. Rich, M. Seshadri, Photoacoustic imaging of vascular hemodynamics: Validation with blood oxygenation level-dependent MR imaging. *Radiology* **275**, 110–118 (2015).
27. I. Quiros-Gonzalez, M. R. Tomaszewski, S. J. Aitken, L. Ansel-Bollepalli, L. A. McDuffus, M. Gill, L. Hacker, J. Brunker, S. E. Bohndiek, Optoacoustics delineates murine breast cancer models displaying angiogenesis and vascular mimicry. *Br. J. Cancer* **118**, 1098–1106 (2018).
28. E. Brown, J. Brunker, S. E. Bohndiek, Photoacoustic imaging as a tool to probe the tumour microenvironment. *Dis. Model. Mech.* **12**, dmm039636 (2019).
29. G. Balasundaram, L. Ding, X. Li, A. B. E. Attia, X. L. Dean-Ben, C. J. H. Ho, P. Chandrasekharan, H. C. Tay, H. Q. Lim, C. B. Ong, R. P. Mason, D. Razansky, M. Olivo, Noninvasive anatomical and functional imaging of orthotopic glioblastoma development and therapy using multispectral optoacoustic tomography. *Transl. Oncol.* **11**, 1251–1258 (2018).
30. S. Goel, J. de la-Cerda, W. Schuler, A. Kotrotsou, J. Cardenas-Rodriguez, M. Pagel, "Evaluations of radiotherapy in small animal models of pancreatic cancer with oxygen enhanced–dynamic contrast enhanced multispectral optoacoustic tomography (OE-DCE MSOT)" in *Proceedings of SPIE* (SPIE, 2023), vol. 12379, pp. 123791B.
31. J. A. Carr, D. Franke, J. R. Caram, C. F. Perkinson, M. Saif, V. Askoxylakis, M. Datta, D. Fukumura, R. K. Jain, M. G. Bawendi, O. T. Bruns, Shortwave infrared fluorescence imaging with the clinically approved near-infrared dye indocyanine green. *Proc. Natl. Acad. Sci. U.S.A.* **115**, 4465–4470 (2018).
32. A. Rovini, K. A. Heslop, E. N. Maldonado, "6.25 - Mitochondria and tumor metabolic flexibility: Mechanisms and therapeutic perspectives" in *Comprehensive Pharmacology*, T. Kenakin, Ed. (Elsevier, 2022), pp. 493–510.
33. M. E. Carter-Timofte, R. Arulanandam, N. Kurmasheva, K. Fu, G. Laroche, Z. Taha, D. van der Horst, L. Cassin, R. M. van der Sluis, E. Palermo, D. Di Carlo, D. Jacobs, G. Maznyi, T. Azad, R. Singaravelu, F. Ren, A. L. Hansen, M. Idorn, C. K. Holm, M. R. Jakobsen, J. van Grevenynghe, J. Hiscott, S. R. Paludan, J. C. Bell, J. Seguin, L. A. Sabourin, M. Côté, J. S. Diallo, T. Alain, D. Olagnier, Antiviral potential of the antimicrobial drug atovaquone against SARS-CoV-2 and emerging variants of concern. *ACS. Infect. Dis.* **7**, 3034–3051 (2021).
34. Q. Lu, W. Gao, Z. Chen, Z. Liu, J. Wang, L. Zeng, X. Hu, E. Zheng, Q. Zhang, H. Song, Co-delivery of Paclitaxel/Atovaquone/Quercetin to regulate energy metabolism to

reverse multidrug resistance in ovarian cancer by PLGA-PEG nanoparticles. *Int. J. Pharm.* **655**, 124028 (2024).
35. N. Sommer, N. Alebrahimdehkordi, O. Pak, F. Knoepp, I. Strielkov, S. Scheibe, E. Dufour, A. Andjelković, A. Sydykov, A. Saraji, A. Petrovic, K. Quanz, M. Hecker, M. Kumar, J. Wahl, S. Kraut, W. Seeger, R. T. Schermuly, H. A. Ghofrani, K. Ramser, T. Braun, H. T. Jacobs, N. Weissmann, M. Szibor, Bypassing mitochondrial complex III using alternative oxidase inhibits acute pulmonary oxygen sensing. *Sci. Adv.* **6**, eaba0694 (2020).
36. M. Bajzikova, J. Kovarova, A. R. Coelho, S. Boukalova, S. Oh, K. Rohlenova, D. Svec, S. Hubackova, B. Endaya, K. Judasova, A. Bezawork-Geleta, K. Kluckova, L. Chatre, R. Zobalova, A. Novakova, K. Vanova, Z. Ezrova, G. J. Maghzal, S. Magalhaes Novais, M. Olsinova, L. Krobova, Y. J. An, E. Davidova, Z. Nahacka, M. Sobol, T. Cunha-Oliveira, C. Sandoval-Acuña, H. Strnad, T. Zhang, T. Huynh, T. L. Serafim, P. Hozak, V. A. Sardao, W. J. H. Koopman, M. Ricchetti, P. J. Oliveira, F. Kolar, M. Kubista, J. Truksa, K. Dvorakova-Hortova, K. Pacak, R. Gurlich, R. Stocker, Y. Zhou, M. V. Berridge, S. Park, L. Dong, J. Rohlena, J. Neuzil, Reactivation of dihydroorotate dehydrogenase-driven pyrimidine biosynthesis restores tumor growth of respiration-deficient cancer cells. *Cell Metab.* **29**, 399–416.e10 (2019).
37. P. Ghosh, Y. Guo, A. Ashrafi, J. Chen, S. Dey, S. Zhong, J. Liu, J. Campbell, P. C. Konduri, J. Gerberich, M. Garrossian, R. P. Mason, L. Zhang, L. Liu, Oxygen-enhanced optoacoustic tomography reveals the effectiveness of targeting heme and oxidative phosphorylation at normalizing tumor vascular oxygenation. *Cancer Res.* **80**, 3542–3555 (2020).
38. M. R. Tomaszewski, I. Q. Gonzalez, J. P. O'Connor, O. Abeyakoon, G. J. Parker, K. J. Williams, F. J. Gilbert, S. E. Bohndiek, Oxygen enhanced optoacoustic tomography (OE-OT) reveals vascular dynamics in murine models of prostate cancer. *Theranostics* **7**, 2900–2913 (2017).
39. M. R. Tomaszewski, M. Gehrung, J. Joseph, I. Quiros-Gonzalez, J. A. Disselhorst, S. E. Bohndiek, Oxygen-enhanced and dynamic contrast-enhanced optoacoustic tomography provide surrogate biomarkers of tumor vascular function, hypoxia, and necrosis. *Cancer Res.* **78**, 5980–5991 (2018).
40. A. V. Silva, U. Norinder, E. Liiv, B. Platzack, M. Öberg, E. Törnqvist, Associations between clinical signs and pathological findings in toxicity testing. *ALTEX* **38**, 198–214 (2021).
41. J. Fillingham, M.-C. Keogh, N. J. Krogan, γ H2AX and its role in DNA double-strand break repair. *Biochem. Cell Biol.* **84**, 568–577 (2006).
42. S. Goel, D. G. Duda, L. Xu, L. L. Munn, Y. Boucher, D. Fukumura, R. K. Jain, Normalization of the vasculature for treatment of cancer and other diseases. *Physiol. Rev.* **91**, 1071–1121 (2011).
43. M. Kanehisa, Toward understanding the origin and evolution of cellular organisms. *Protein Sci.* **28**, 1947–1951 (2019).
44. T. Cardilin, J. Almquist, M. Jirstrand, A. Zimmermann, F. Lignet, S. El Bawab, J. Gabrielsson, Modeling long-term tumor growth and kill after combinations of radiation and radiosensitizing agents. *Cancer Chemother. Pharmacol.* **83**, 1159–1173 (2019).
45. T. Cardilin, J. Almquist, M. Jirstrand, J. Gabrielsson, Evaluation and translation of combination therapies in oncology – A quantitative approach. *Eur. J. Pharmacol.* **834**, 327–336 (2018).
46. T. Cardilin, J. Almquist, M. Jirstrand, A. Sostelly, C. Amendt, S. El Bawab, J. Gabrielsson, Tumor static concentration curves in combination therapy. *AAPS J.* **19**, 456–467 (2017).
47. K. Nemes, M. C. Frühwald, Emerging therapeutic targets for the treatment of malignant rhabdoid tumors. *Expert Opin. Ther. Targets* **22**, 365–379 (2018).
48. D. Chen, X. Sun, X. Zhang, J. Cao, Targeting mitochondria by anthelmintic drug atovaquone sensitizes renal cell carcinoma to chemotherapy and immunotherapy. *J. Biochem. Mol. Toxicol.* **32**, e22195 (2018).
49. Z. Lv, X. Yan, L. Lu, C. Su, Y. He, Atovaquone enhances doxorubicin's efficacy via inhibiting mitochondrial respiration and STAT3 in aggressive thyroid cancer. *J. Bioenerg. Biomembr.* **50**, 263–270 (2018).
50. A. M. Stevens, M. Xiang, L. N. Heppler, I. Tošić, K. Jiang, J. O. Munoz, A. S. Gaikwad, T. M. Horton, X. Long, P. Narayanan, E. L. Seashore, M. C. Terrell, R. Rashid, M. J. Krueger, A. E. Mangubat-Medina, Z. T. Ball, P. Sumazin, S. R. Walker, Y. Hamada, S. Oyadomari, M. S. Redell, D. A. Frank, Atovaquone is active against AML by upregulating the integrated stress pathway and suppressing oxidative phosphorylation. *Blood Adv.* **3**, 4215–4227 (2019).
51. A. Muscat, D. Popovski, W. S. N. Jayasekara, F. J. Rossello, M. Ferguson, K. D. Marini, M. Alamgeer, E. M. Algar, P. Downie, D. N. Watkins, J. E. Cain, D. M. Ashley, Low-dose histone deacetylase inhibitor treatment leads to tumor growth arrest and multi-lineage differentiation of malignant rhabdoid tumors. *Clin. Cancer Res.* **22**, 3560–3570 (2016).
52. T. P. Howard, T. E. Arnoff, M. R. Song, A. O. Giacomelli, X. Wang, A. L. Hong, N. V. Dharia, S. Wang, F. Vazquez, M.-T. Pham, A. M. Morgan, F. Wachter, G. H. Bird, G. Kugener, E. M. Oberlick, M. G. Rees, H. L. Tiv, J. H. Hwang, K. H. Walsh, A. Cook, J. M. Krill-Burger, A. Tsherniak, P. C. Gokhale, P. J. Park, K. Stegmaier, L. D. Walensky, W. C. Hahn, C. W. M. Roberts, MDM2 and MDM4 are therapeutic vulnerabilities in malignant rhabdoid tumors. *Cancer Res.* **79**, 2404–2414 (2019).
53. S. David, P. Y. Kim, "Drug trials" in *StatPearls* (StatPearls Publishing, 2024).
54. T. M. Ashton, W. G. McKenna, L. A. Kunz-Schughart, G. S. Higgins, Oxidative phosphorylation as an emerging target in cancer therapy. *Clin. Cancer Res.* **24**, 2482–2490 (2018).
55. T. A. Yap, N. Daver, M. Mahendra, J. Zhang, C. Kamiya-Matsuoka, F. Meric-Bernstam, H. M. Kantarjian, F. Ravandi, M. E. Collins, M. E. D. Francesco, E. E. Dumbrava, S. Fu, S. Gao, J. P. Gay, S. Gera, J. Han, D. S. Hong, E. J. Jabbour, Z. Ju, D. D. Karp, A. Lodi, J. R. Molina, N. Baran, A. Naing, M. Ohanian, S. Pant, N. Pemmaraju, P. Bose, S. A. Piha-Paul, J. Rodon, C. Salguero, K. Sasaki, A. K. Singh, V. Subbiah, A. M. Tsimberidou, Q. A. Xu, M. Yilmaz, Q. Zhang, Y. Li, C. A. Bristow, M. B. Bhattacharjee, S. Tiziani, T. P. Heffernan, C. P. Vellano, P. Jones, C. J. Heijnen, A. Kavelaars, J. R. Marszalek, M. Konopleva, Complex I inhibitor of oxidative phosphorylation in advanced solid tumors and acute myeloid leukemia: Phase I trials. *Nat. Med.* **29**, 115–126 (2023).
56. M. Pujalte-Martin, A. Belaïd, S. Bost, M. Kahi, P. Peraldi, M. Rouleau, N. M. Mazure, F. Bost, Targeting cancer and immune cell metabolism with the complex I inhibitors metformin and IACS-010759. *Mol. Oncol.* **18**, 1719–1738 (2024).
57. I. Mahmood, Dosing in children: A critical review of the pharmacokinetic allometric scaling and modelling approaches in paediatric drug development and clinical settings. *Clin. Pharmacokinet.* **53**, 327–346 (2014).
58. L. Mohr, M. Carceles-Cordon, J. Woo, C. Cordon-Cardo, J. Domingo-Domenech, V. Rodriguez-Bravo, Generation of prostate cancer cell models of resistance to the anti-mitotic agent docetaxel. *J. Vis. Exp.* **8**, e56327 (2017).
59. J. Falloon, S. Sargent, S. C. Piscitelli, C. Bechtel, S. W. LaFon, B. Sadler, R. E. Walker, J. A. Kovacs, M. A. Polis, R. T. Davey Jr., H. C. Lane, H. Masur, Atovaquone suspension in HIV-infected volunteers: Pharmacokinetics, pharmacodynamics, and TMP-SMX interaction study. *Pharmacotherapy* **19**, 1050–1056 (1999).
60. G. L. Nixon, D. M. Moss, A. E. Shone, D. G. Lalloo, N. Fisher, P. M. O'Neill, S. A. Ward, G. A. Biagini, Antimalarial pharmacology and therapeutics of atovaquone. *J. Antimicrob. Chemother.* **68**, 977–985 (2013).
61. R. Dixon, A. Pozniak, H. Watt, P. Rolan, J. Posner, Single-dose and steady-state pharmacokinetics of a novel microfluidized suspension of atovaquone in human immunodeficiency virus-seropositive patients. *Antimicrob. Agents Chemother.* **40**, 556–560 (1996).
62. C. W. Hupple, S. Morscher, N. C. Burton, M. D. Pagel, L. R. McNally, J. Cárdenas-Rodríguez, A light-fluence-independent method for the quantitative analysis of dynamic contrast-enhanced multispectral optoacoustic tomography (DCE MSOT). *Photoacoustics* **10**, 54–64 (2018).
63. B. De, P. Dogra, M. Zaid, D. Elganainy, K. Sun, A. M. Amer, C. Wang, M. K. Rooney, E. Chang, H. C. Kang, Z. Wang, P. Bhosale, B. C. Odisio, T. E. Newhook, C. D. Tzeng, H. S. T. Cao, Y. S. Chun, J. N. Vauthey, S. S. Lee, A. Kaseb, K. Raghav, M. Javle, B. D. Minsky, S. S. Noticewala, E. B. Holliday, G. L. Smith, A. C. Koong, P. Das, V. Cristini, E. B. Ludmir, E. J. Koay, Measurable imaging-based changes in enhancement of intrahepatic cholangiocarcinoma after radiotherapy reflect physical mechanisms of response. medRxiv 24313334 [Preprint] (2024).
64. P. Dogra, J. R. Ramírez, J. D. Butner, M. J. Peláez, C. Chung, A. Hooda-Nehra, R. Pasqualini, W. Arap, V. Cristini, G. A. Calin, B. Ozpolat, Z. Wang, Translational modeling identifies synergy between nanoparticle-delivered miRNA-22 and standard-of-care drugs in triple-negative breast cancer. *Pharm. Res.* **39**, 511–528 (2022).
65. P. Dogra, V. Shinglot, J. Ruiz-Ramírez, J. Cave, J. D. Butner, C. Schiavone, D. G. Duda, A. O. Kaseb, C. Chung, E. J. Koay, V. Cristini, B. Ozpolat, G. A. Calin, Z. Wang, Translational modeling-based evidence for enhanced efficacy of standard-of-care drugs in combination with anti-microRNA-155 in non-small-cell lung cancer. *Mol. Cancer* **23**, 156 (2024).
66. World Health Organization, Measles vaccines: WHO position paper, April 2017 – Recommendations. *Vaccine* **37**, 219–222 (2019).
67. E. A. Eisenhauer, P. Therasse, J. Bogaerts, L. H. Schwartz, D. Sargent, R. Ford, J. Dancey, S. Arbuck, S. Gwyther, M. Mooney, L. Rubinstein, L. Shankar, L. Dodd, R. Kaplan, D. Lacombe, J. Verweij, New response evaluation criteria in solid tumours: Revised RECIST guideline (version 1.1). *Eur. J. Cancer* **45**, 228–247 (2009).
68. E. J. Hall, A. J. Giaccia, *Radiobiology for the Radiologist* (Wolters Kluwer, ed. 8, 2018).
69. G. G. Steel, *Basic Cinical Radiobiology* (Hodder Arnold, ed. 3, 2002).
70. J. B. West, A. M. Luks, *West's Respiratory Physiology* (Lippincott Williams & Wilkins, 2020).
71. P. Vaupel, A. Mayer, Hypoxia in cancer: Significance and impact on clinical outcome. *Cancer Metastasis Rev.* **26**, 225–239 (2007).
72. M. Höckel, P. Vaupel, Tumor hypoxia: Definitions and current clinical, biologic, and molecular aspects. *J. Natl. Cancer Inst.* **93**, 266–276 (2001).
73. P. Vaupel, K. Schlenger, C. Knoop, M. Höckel, Oxygenation of human tumors: Evaluation of tissue oxygen distribution in breast cancers by computerized O2 tension measurements. *Cancer Res.* **51**, 3316–3322 (1991).
74. A. Darade, S. Pathak, S. Sharma, V. Patravale, Atovaquone oral bioavailability enhancement using electrospraying technology. *Eur. J. Pharm. Sci.* **111**, 195–204 (2018).

Acknowledgments: We thank D. H. Lum and T. Yin Chan (Preclinical Research Shared Resource at Huntsman Cancer Institute at the University of Utah) for technical assistance in cell transduction. **Funding:** This work was supported, in part, by the University of Utah College of

Pharmacy (S.G.); the University of Utah Immunology, Inflammation and Infectious Diseases (3i) Initiative (S.G. and S.S.), the 5 For the Fight Fellowship (S.G.), and the Elsa U Pardee Foundation (S.G); the University of Utah School of Medicine (S.S.) and the Office of the Vice President for Research Seed Grant (S.S.) and Research Instrumentation Fund (S.G.); and National Institutes of Health (NIH) grant R01EB035545 (P.D.). We acknowledge direct financial support from the Huntsman Cancer Center supported by the National Cancer Institute of the NIH under award number P30CA042014. The content is solely the responsibility of the authors and does not necessarily represent the official views of the NIH. **Author contributions:** S.G. and S.S. conceived and designed the experiments. W.X. and E.N. performed the experiments and data analysis. P.D. conceived and designed mathematical modeling experiments. C.S. and J.C. performed mathematical modeling. M.G. and N.S. analyzed the MSOT imaging data. J.H. performed ex vivo imaging experiments and data analysis. D.L.G. and R.L.J. provided assistance with x-ray irradiation. M.D.P. and S.G. created the OE-DCE MSOT MATLAB code. W.X., S.G., and P.D. wrote the manuscript. S.G. and S.S. edited the manuscript. **Competing interests:** The authors declare that they have no competing interests. **Data and materials availability:** All data needed to evaluate the conclusions in the paper are present in the paper and/or the Supplementary Materials.

Submitted 18 December 2024
Accepted 18 April 2025
Published 23 May 2025
10.1126/sciadv.adv2930